

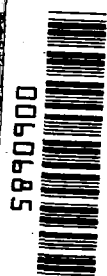
**NASA CONTRACTOR
REPORT**

NASA CR-1846



NASA CR-1

NASA
CR
1525
pt. 2
c. 1



TECH LIBRARY KAFB, NM

LOAN COPY: RET
AFWL (DO4L)
KIRTLAND AFB, N. M.

**THE EFFECT OF COMPOSITION ON
THE MECHANISM OF STRESS-CORROSION
CRACKING OF TITANIUM ALLOYS IN N_2O_4 ,
AND AQUEOUS AND HOT-SALT ENVIRONMENTS
(Part II)**

*by J. D. Boyd, P. J. Moreland, W. K. Boyd,
R. A. Wood, D. N. Williams, and R. I. Jaffee*

Prepared by
BATTELLE MEMORIAL INSTITUTE
Columbus, Ohio 43201
for

NATIONAL AERONAUTICS AND SPACE ADMINISTRATION • WASHINGTON, D. C. • OCTOBER 1971



0060685

1. Report No. NASA CR-1846		2. Government Accession No.		3. Recipient's Catalog No.	
4. Title and Subtitle THE EFFECT OF COMPOSITION ON THE MECHANISM OF STRESS-CORROSION CRACKING OF TITANIUM ALLOYS IN N_2O_4 , AND AQUEOUS AND HOT-SALT ENVIRONMENTS (Part II)				5. Report Date October 1971	
				6. Performing Organization Code	
7. Author(s) J. D. Boyd, P. J. Moreland, W. K. Boyd, R. A. Wood, D. N. Williams, and R. I. Jaffee				8. Performing Organization Report No.	
9. Performing Organization Name and Address Battelle Memorial Institute Columbus Laboratories 505 King Avenue Columbus, Ohio 43201				10. Work Unit No.	
				11. Contract or Grant No. NASr-100(09)	
12. Sponsoring Agency Name and Address National Aeronautics and Space Administration Washington, D. C. 20546				13. Type of Report and Period Covered Contractor Report	
				14. Sponsoring Agency Code	
15. Supplementary Notes					
<p>16. Abstract Experimental alloys were prepared to assess the effects of alloy composition on susceptibility to stress-corrosion cracking in aqueous environments. Some tests were performed on 0.25 and 0.5-inch-thick specimens, with and without side notches, to verify that the critical effect of aluminum concentration is real and not just a consequence of the state of stress at the crack tip. The thicker specimens exhibited slightly lower toughness in air and in salt water, but this was a small effect compared to the dramatic decrease in $K_{I_{sc}}$ observed for alloys containing greater than 6 weight percent aluminum.</p> <p>A detailed metallographic study was made of the morphology of stress-corrosion cracks and of the distribution of slip within the crack-tip plastic zone. These results, and others, are used to formulate a phenomenological model for aqueous stress-corrosion cracking of titanium alloys. Crack velocity data are analyzed in terms of an analytic relationship between crack velocity and applied stress intensity.</p> <p>The stress-corrosion cracking behavior in oxygenated (red) N_2O_4 of a series of experimental alloys containing 5-7 weight percent aluminum was investigated by means of chemical, electro-chemical and fractographic studies. All of the experimental alloys were susceptible in oxygenated (red) N_2O_4 at 250 psig O_2 and 106°F. Alloy composition was found to influence the corrosion resistance and the stress-corrosion fracture mode.</p>					
17. Key Words (Suggested by Author(s)) Stress-corrosion cracking Titanium				18. Distribution Statement Unclassified - Unlimited	
19. Security Classif. (of this report) Unclassified		20. Security Classif. (of this page) Unclassified		21. No. of Pages 78	
				22. Price* \$3.00	

TABLE OF CONTENTS

TABLES	Page iv
FIGURES	v
SUMMARY	ix
LIST OF SYMBOLS	xi
TESTING OF EXPERIMENTAL ALLOYS	1
Introduction	1
Materials Preparation	1
Tensile and Creep Tests	1
Aqueous Stress-Corrosion Tests	7
MECHANISMS OF STRESS-CORROSION CRACKING	19
Aqueous Environments	19
Introduction	19
Experimental	20
Material	20
Specimen Geometry and Testing Procedure	20
Metallography	22
Fractography	24
Results	24
Crack-Velocity Measurements	24
Crack-Tip Morphologies	25
Fractography	32
Studies of Crack-Tip Plastic Zones	32
Discussion	35
General Observations	35
Analysis of Crack-Velocity Data	40
Observations of Crack-Tip Morphologies	49
Crack-Tip Plastic Zones	52
N ₂ O ₄ Environments	53
Chemical Studies	53
Electrochemical Studies	55
Fractographic Studies	57
6.5 to 7 Al-Base Alloys	57
5 to 6 Al-Base Alloys	61
Summary	65
REFERENCES	67

LIST OF TABLES

<u>Tables</u>	<u>Page</u>
1. Compositions of Alloys Obtained for Third-Year Study	2
2. Fabrication Schedule for Experimental Alloys Obtained for Third-Year Study	3
3. Beta-Transus and Solution-Heat-Treatment Temperatures Used for Alloys of Third-Year Study	4
4. Room-Temperature Tensile Properties for Experimental Alloys as Annealed	5
5. 600 F Creep Data and Room-Temperature Tensile Properties of Experimental Alloys before and After 600 F Creep Exposure	7
6. Fracture-Toughness Data Obtained for 0.125-Inch-Thick Specimens in Air and 3.5 Percent NaCl Solution	9
7. Fracture-Toughness Data Obtained for 0.250-Inch-Thick Specimen in Air and 3.5 Percent NaCl Solution	11
8. Fracture-Toughness Data Obtained for 0.250-Inch-Thick Side-Notched Specimen in 3.5 Percent NaCl Solution	12
9. Measured Slip-Step Heights and Slip-Band Spacings	36
10. Typical Values of Fracture Toughness and Subcritical-Crack Velocity for Selected Materials and Environments	39
11. Summary of Data on Crack Velocities for Ti-Al-1Mo-1V	45
12. Composition, Weight Percent, of Experimental Alloys Exposed to N_2O_4	53
13. Weight Loss of Titanium Alloys Exposed to Oxygenated N_2O_4 at 250 PSIG O_2 and 106 F	55

LIST OF FIGURES

<u>Figures</u>	<u>Page</u>
1. Specimen Geometry, Sheet Tensile and Sheet Creep Specimens	6
2. Geometry of Precracked Cantilever Test Specimen	8
3. Geometry of Side-Notched Specimens	13
4. Geometry of 1/2-Inch-Thick Specimens, Cantilever Notch Bend Test	14
5. Effect of Aluminum Content on the Strength, Toughness, and Stress-Corrosion Susceptibility of Ti-1.5Mo-0.5V-Base Alloys	15
6. Effect of Oxygen Content on the Toughness and Stress-Corrosion Susceptibility of Ti-(6,6.5,7)Al-1.5Mo-0.5V Alloys	17
7. Effect of Beta Stabilizer Amount and Kind on Yield Strength, Toughness, and Stress-Corrosion Susceptibility of Ti-6Al Base Alloys (1000 PPM O ₂)	18
8. Specimen Geometry and Loading Arrangement	21
9. Calibration Chart for Crack Velocity Measurements	23
10. Subcritical-Crack Velocities for Ti-8Al-1Mo-1V, in 3.5 Percent NaCl, at Room Temperature	24
11. Effect of Environment Temperature on Subcritical-Crack Velocities	26
12. Effect of Bulk Chloride-Ion Concentration on Subcritical-Crack Velocities	26
13. Variation in Crack-Tip Morphology with Distance from Surface of Specimen (d)	27
14. Details of Two Different Crack-Tip Morphologies	28
15. A Through-Thickness Series of Micrographs Showing the Width of Severely Branched-Crack Segments	30
16. Scanning Electron Micrograph of an Area of Rapid Fracture	31
17. Scanning Electron Micrographs from Areas of Stress-Corrosion Fracture	33
18. Electron Micrograph of a Two-Stage Carbon Replica, Illustrating the Distribution of Slip Around A Stress-Corrosion Crack	34
19. Nonhomogeneous Slip in the Plastic Zone of a Stress-Corrosion Crack	35

LIST OF FIGURES (Cont'd)

20.	Calculation of Slip-Step Height, h , from Slip-Line Width, w	37
21.	Idealized Variation in Cleavage Strength with Concentration of Embrittling Species	41
22.	Variation in $K_{I_{sc}}$ With Yield Stress for Ti-Al Base Alloys	43
23.	Idealized Crack Tip	44
24.	Temperature Dependence of S_o	46
25.	Variation in S_o With Chloride-Ion Concentration	46
26.	Temperature Dependence of A°	47
27.	Variation in A° With Chloride-Ion Concentration	47
28.	Schematic Illustration of the Front of a Propagating Stress Corrosion Crack During State II	51
29.	Sem Fractograph of Ti-7Al-0.1 O Alloy	58
30.	Sem Fractograph of Ti-75A Alloy	58
31.	Photomicrograph of Ti-7Al-0.1 O Alloy	58
32.	Surface Fractograph of Ti-75A Alloy	58
33.	Sem Surface Photomicrograph of Ti-7Al-0.1 O Alloy	59
34.	Sem Fractograph of Ti-6.5Al-1.5Mo-0.5V-0.1 O Alloy	59
35.	Sem Fractograph of Ti-6.5Al-1.5Mo-0.5V-0.22 O Alloy	59
36.	Sem Surface Fractograph of Ti-7Al-1.5Mo-0.5V-0.1 O Alloy	60
37.	Photomicrograph of Ti-7Al-1.5Mo-0.5V-0.23 O Alloy	60
38.	Sem Fractograph of Ti-7Al-1.5Mo-0.5V-0.2Pd Alloy	60
39.	Photomicrograph of Ti-7Al-1.5Mo-0.5V-0.2Pd Alloy	60
40.	Sem Fractograph of Ti-7Al-2V-0.1 O Alloy	62
41.	Sem Fractograph of Ti-7Al-2Mn-0.1 O Alloy	62
42.	Sem Fractograph of Ti-6Al-4V Alloy in the STA Condition	62
43.	Photomicrograph of Ti-6Al-4V Alloy in the STA Condition	62

LIST OF FIGURES (Cont'd)

44.	Sem Surface Fractograph of Ti-6Al-4V Alloy in STA Condition	63
45.	Sem Fractograph of Ti-6Al-0.1 O Alloy	63
46.	Sem Fractograph of Ti-6Al-1.5Mo-0.5V-0.1 O Alloy	63
47.	Sem Fractograph of Ti-5Al-1.5Mo-0.5V 0.1 O Alloy	64
48.	Sem Fractograph of Ti-6Al-2V-0.1 O Alloy	64
49.	Sem Fractograph of Ti-6Al-1.5Mo-0.5V-0.18 O Alloy	64

SUMMARY

This report describes work performed during the third year of Contract No. NASr-100(09), (May 1, 1969-April 30, 1970).

The research program consisted of 3 concurrent phases: (1) Characterization and Evaluation of Experimental Alloys, (2) Mechanisms of Stress-Corrosion Cracking in Aqueous Environments, (3) Mechanisms of Stress-Corrosion in N_2O_4 Environments. The results are discussed under these 3 headings, although there was some overlap among the various phases.

Characterization and Evaluation of Experimental Alloys

Ten new experimental alloys were prepared to further assess the effects of alloy composition on susceptibility to stress-corrosion cracking in aqueous environments. The new compositions contained 5-6 weight percent aluminum with various oxygen and beta-stabilizer contents. Some tests were performed on 0.25 and 0.5-inch-thick specimens, with and without side notches, to verify that the critical effect of aluminum concentration is real and not just a consequence of the state of stress at the crack tip. The thicker specimens exhibited slightly lower toughness in air and in salt water, but this was a small effect compared to the dramatic decrease in $K_{I_{SCC}}$ observed for alloys containing greater than 6 weight percent aluminum.

Mechanisms of Stress-Corrosion Cracking in Aqueous Environments

A detailed metallographic study was made of the morphology of stress-corrosion cracks and of the distribution of slip within the crack-tip plastic zone. These results, the results of earlier work on this program, and the results of other workers have been used to formulate a phenomenological model for aqueous stress-corrosion cracking of titanium alloys. In addition, the crack velocity data reported earlier have been re-analyzed in terms of an analytic relationship between crack velocity and applied stress intensity. These data will be used to test quantitative results when they are available.

Mechanisms of Stress-Corrosion Cracking in N_2O_4 Environments

The stress-corrosion cracking behavior in oxygenated (red) N_2O_4 of a series of experimental alloys containing 5-7 weight percent aluminum has been investigated by means of chemical, electrochemical and fractographic studies. All of the experimental alloys were susceptible to stress-corrosion cracking in oxygenated (red) N_2O_4 at 250 psig O_2 and 106°F. Alloy composition was found to markedly influence the corrosion resistance and the stress-corrosion fracture mode. Corrosion resistance was found to decrease with increasing additions of molybdenum, vanadium, and oxygen. The effect of molybdenum and vanadium, thus, typified the general corrosion behavior of these alloying elements in oxidizing environments. Aluminum content had no significant effect on the corrosion resistance of the alloys, but the α alloys Ti-6Al-0.1 O and Ti-7Al-0.1 O did show good corrosion resistance. The most corrosion-resistant alloy was Ti-7Al-2Mn-0.1 O. This alloy, which also exhibited an initial slow crack growth, represented the most resistant alloy to stress-corrosion cracking in oxygenated (red) N_2O_4 .

LIST OF SYMBOLS

σ	applied tensile stress
σ_f^*	intrinsic cleavage stress of pure metal
σ^*	cleavage stress of metal when the concentration of embrittling species is X^*
σ_i^*	minimum cleavage stress for metal-x system which obtains for $X^* \geq X_i^*$
Y	tensile yield stress
ϵ	uniaxial strain
$\dot{\epsilon}$	uniaxial strain rate
K, K_I	applied stress intensity
K_C	fracture toughness (mixed mode or plane stress)
K_{I_C}	plane-strain fracture toughness
K_{I_X}	applied stress intensity at fracture
$K_{I_{scc}}$	minimum stress intensity for propagation of a stress-corrosion crack
$K_{I_f}^*$	critical applied stress intensity for cleavage of pure metal
K_I^*	critical applied stress intensity for cleavage when the concentration of embrittling species is X^*
$K_{I_i}^*$	minimum applied stress intensity for cleavage in the metal-x system which obtains for $X^* \geq X_i^*$
K_{I_B}	applied stress intensity when $\dot{a} = \dot{a}^0$
a	crack length
\dot{a}	crack velocity
\dot{a}^0	limiting crack velocity
ρ	length of crack-tip plastic zone
C	crack-opening displacement
B	specimen thickness
D	specimen depth

M	bending moment at crack plane
d	distance from specimen surface measured in the through-thickness direction
X_{Cl^-}	concentration of Cl^- ions in the electrolyte
J	flux of embrittling species into crack-tip plastic zone
T	absolute temperature
S_o	initial slope of $\bar{a}-K_I$ curve
Q_{β}^H	activation energy for diffusion of hydrogen in beta titanium
h	slip-step height
w	slip-line width
ϕ	angle of incidence of shadowing material
θ	angle between slip line and projection of shadowing direction on specimen surface

THE EFFECT OF COMPOSITION ON THE MECHANISM OF STRESS-CORROSION CRACKING OF TITANIUM ALLOYS IN N_2O_4 , AND AQUEOUS AND HOT-SALT ENVIRONMENTS

by

J. D. Boyd, P. J. Moreland, W. K. Boyd, R. A. Wood,
D. N. Williams, and R. I. Jaffee

TESTING OF EXPERIMENTAL ALLOYS

Introduction

The first 2 years' work on this program showed that the composition of the alpha phase in beta-lean, alpha-plus-beta alloys, largely determines the aqueous stress-corrosion susceptibility of an alloy. The amount or kind of beta-stabilizer addition has a small effect on susceptibility compared with that of aluminum-plus-oxygen alpha-stabilizer content. Nevertheless, there are some important considerations to be given to which beta-stabilizer addition should be combined with a critical aluminum-plus-oxygen alpha addition to result in the highest performance alloy - performance based on mechanical properties plus an immunity to aqueous stress-corrosion cracking. Thus the third-year work on this program was aimed at refining the knowledge of what constitutes critical alpha-stabilizer content and auxiliary beta-stabilizer effects. Toward this end, several alloys containing aluminum-plus-oxygen additions in the range of the critical amount, augmented with a preferred beta-stabilizer content, were evaluated.

Materials Preparation

The ten experimental alloys for the present study were obtained from the Titanium Metals Corporation of America in the form of double-melted 22-pound ingots. The manufacturers' analyses are given in Table 1. These materials were fabricated to 0.25-inch plate and 0.125-inch sheet according to the schedule given in Table 2. The beta-transus temperature was determined metallographically as in previous work⁽¹⁻³⁾, and a suitable solution-annealing temperature was selected for each alloy. Beta-transus temperatures and solution temperatures are given in Table 3. The solution-annealing treatment was terminated by furnace cooling at 100 F/hour to 1200 F, holding for 1 hour at 1200 F and air cooling to room temperature. This schedule was followed by vacuum annealing at 1200 F for 3 to 4 hours, terminated by chamber cooling. This procedure reduces hydrogen content in materials to a low level and puts material prone to stress corrosion into a susceptible condition.

Tensile and Creep Tests

The room-temperature tensile data obtained for this series of alloys are given in Table 4. Sample geometry is shown in Figure 1. The annealed strength and ductility combinations appear to be quite regular for compositions of this type.

TABLE 1. COMPOSITIONS OF ALLOYS OBTAINED FOR THIRD-YEAR STUDY^(a)

Vendor Heat	Nominal Composition, percent				Analytical Results, percent				
	Al	Mo	V	O	Al	Mo	V	Fe	N
V-4177	5	1.5	0.5	0.10	5.04	1.37	0.47	0.031	0.004
V-4178	5.5	1.5	0.5	0.10	5.30	1.34	0.48	0.031	0.006
V-4179	6	1.5	0.5	0.05	5.93	1.31	0.53	0.017	0.006
V-4180	6	1.5	0.5	0.10	5.78	1.32	0.53	0.029	0.007
V-4181	6	1.5	0.5	0.18	5.71	1.33	0.53	0.029	0.006
V-4182	6.5	1.5	0.5	0.05	6.42	1.38	0.59	0.031	0.004
V-4183	6	--	--	0.10	5.97	--	--	0.024	0.006
V-4184	6	2	--	0.10	6.22	1.89	--	0.037	0.004
V-4185	6	--	2	0.10	6.07	--	2.02	0.069	0.007
V-4186	6	--	4	0.10	6.03	--	4.05	0.074	0.006

(a) In the form of 22 to 25-pound ingots as machined to 4.375-inch diameter.

TABLE 2. FABRICATION SCHEDULE FOR EXPERIMENTAL ALLOYS OBTAINED FOR
THIRD-YEAR STUDY(a)

Alloy	Composition(b), weight percent	Press Forging Temp(c), F	Cross and Direct Rolling to 8-Inch Width(d)		Direct Rolling Temp, F			Fabrication Rating
			Temp, F	Thickness, inch	To 1/2 Inch Thick(d)	To 1/4 Inch Thick(e)	To 1/8 Inch Thick	
177	Ti-5Al-1.5Mo-0.5V	1900	1800	0.915	1700	1700	1600	Good
178	Ti-5.5Al-1.5Mo-0.5V	1900	1800	0.915	1700	1700	1600	Good
179	Ti-6Al-1.5Mo-0.5V (Low oxygen)	1900	1800	0.915	1700	1700	1625	Good
180	Ti-6Al-1.5Mo-0.5V	1900	1800	0.910	1700	1700	1650	Good
181	Ti-6Al-1.5Mo-0.5V (High oxygen)	1900	1800	0.915	1700	1750	1675	Good
182	Ti-6.5Al-1.5Mo-0.5V (Low oxygen)	1900	1800	0.920	1700	1750	1675	Good
183	Ti-6Al	1900	1800	0.925	1700	1750	1675	Poor(f)
184	Ti-6Al-2Mo	1900	1800	0.910	1700	1700	1650	Good
185	Ti-6Al-2V	1900	1800	0.915	1700	1700	1650	Good
186	Ti-6Al-4V	1900	1800	0.900	1700	1700	1625	Good

(a) 22 to 25-pound ingots at 4.375-inch diameter.

(b) 0.10 percent oxygen except as indicated.

(c) Draw-down-type forging (not upset) to 2-inch thickness. Surfaces machined to 0.1-inch depth.

(d) All material subsequently rolled to 0.25-inch thickness with appropriate intermediate conditioning.

(e) One-half length of 0.25-inch plates subsequently rolled to 0.125-inch sheet.

(f) Major cracks resulted from press forging. After conditioning, parts of the billet were rolled to sheet without difficulty.

TABLE 3. BETA-TRANSUS AND SOLUTION-HEAT-TREATMENT TEMPERATURES USED FOR ALLOYS OF THIRD-YEAR STUDY

Alloy	Composition ^(a) , weight percent	Test-Temperature Range ^(b) , 25 F Increments	Beta-Transus Temperature, F	Solution Annealing Temperature, F
177	Ti-5Al-1.5Mo-0.5V	1650-1925 F	1785	1700
178	Ti-5.5Al-1.5Mo-0.5V	1650-1925 F	1770	1725
179	Ti-6Al-1.5Mo-0.5V (Low oxygen)	1650-1925 F	1770	1725
180	Ti-6Al-1.5Mo-0.5V	1700-1975 F	1790	1725
181	Ti-6Al-1.5Mo-0.5V (High oxygen)	1700-2000 F	1835	1750
182	Ti-6.5Al-1.5Mo-0.5V (Low oxygen)	1700-1975 F	1830	1750
183	Ti-6Al	1700-1975 F	1835	1750
184	Ti-6Al-2Mo	1700-1975 F	1820	1750
185	Ti-6Al-2V	1675-1950 F	1790	1725
186	Ti-6Al-4V	1650-1925 F	1735	1675

(a) Nominally 0.10 percent oxygen except as indicated.

(b) Exposure was for 40 minutes in argon, water quench.

TABLE 4. ROOM-TEMPERATURE TENSILE PROPERTIES FOR EXPERIMENTAL ALLOYS AS ANNEALED

(Transverse Samples)

Alloy	Composition(a), weight percent	Yield Stress(b), ksi	Ultimate Stress, ksi	Elongation(c), percent	Reduction in Area, percent
177	Ti-5Al-1.5Mo-0.5V	117.4	120.0	14	28
		116.3	119.1	13	29
178	Ti-5.5Al-1.5Mo-0.5V	113.1	121.6	15	30
		116.6	120.2	17	31
179	Ti-6Al-1.5Mo-0.5V (low oxygen)	116.6	121.4	13	22
		113.9	119.8	15	26
180	Ti-6Al-1.5Mo-0.5V	120.9	127.2	14	33
		124.0	128.2	13	32
181	Ti-6Al-1.5Mo-0.5V (high oxygen)	135.6	143.5	13	27
		134.2	143.8	13	29
182	Ti-6.5Al-1.5Mo-0.5V (low oxygen)	127.5	135.2	13	27
		127.4	134.3	12	27
183	Ti-6Al	87.6	94.1	17	25
		87.7	94.6	17	25
184	Ti-6Al-2Mo	133.4	140.2	15	31
		134.1	142.1	11	19
185	Ti-6Al-2V	125.7	129.9	12	23
		120.0	127.4	12	23
186	Ti-6Al-4V	119.2	129.8	14	39
		122.3	130.0	14	37

(a) 0.10 percent oxygen except as indicated.

(b) 0.2 percent offset yield stress.

(c) Percent elongation in 1 inch.

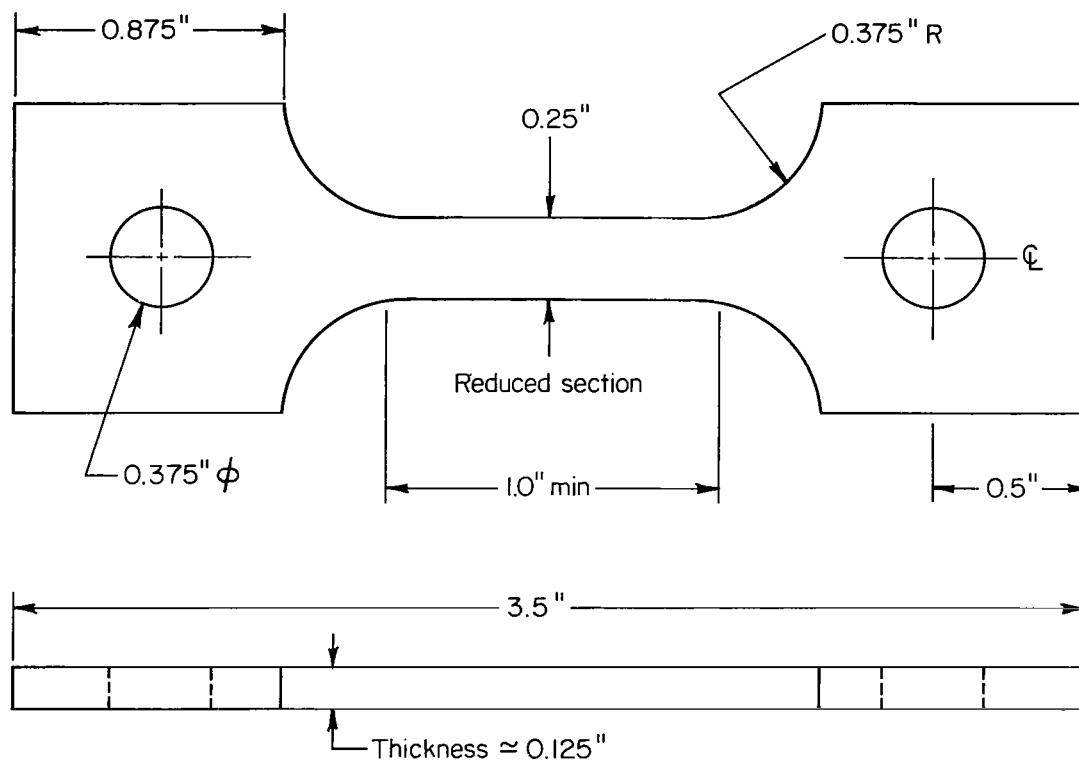


FIGURE 1. SPECIMEN GEOMETRY, SHEET TENSILE AND SHEET CREEP SPECIMENS

Profile surfaces machined; sheet surfaces ground.

Four compositions also were tensile tested after 600 F creep exposure to afford an indication of the materials' thermal stability. The data generated in this test are given in Table 5. It is evident that since a prior creep exposure has such a pronounced effect on tensile elongation, the materials may be considered metallurgically unstable. On the other hand, the observed effect may be a surface oxidation effect since the discoloration due to creep exposure was not removed prior to tensile testing. This appears likely, since in prior work when higher aluminum content alloys were skinned between creep and tensile testing, there was no evidence of instability⁽¹⁾. Further, in the present test, fractures were ductile, with considerable elongation and reduction in area in the fracture region.

TABLE 5. 600 F CREEP DATA AND ROOM-TEMPERATURE TENSILE PROPERTIES OF EXPERIMENTAL ALLOYS BEFORE AND AFTER 600 F CREEP EXPOSURE

(Transverse Specimens)

Alloy	Composition, weight percent	600 F Creep Exposure ^(a)		Total Plastic Strain, percent	Room-Temperature Tensile Data ^(b)			
		Stress, ksi	Time, hours		Yield Stress ^(c) , ksi	Ultimate Stress, ksi	Elongation ^(d) , percent	Reduction in Area, percent
177	Ti-5Al-1.5Mo-0.5V-0.1 O ₂	None	--	--	116.8	119.6	13.5	28.5 ^(e)
		69	71.6	0.294	117.3	122.6	7.0	32.0
178	Ti-5.5Al-1.5Mo-0.5V-0.1 O ₂	None	--	--	114.8	120.9	16.0	30.5 ^(e)
		71	91.0	0.247	117.8	125.4	6.0	28.0
180	Ti-6Al-1.5Mo-0.5V-0.1 O ₂	None	--	--	122.4	127.7	13.5	32.5 ^(e)
		73	73.4	0.170	119.7	129.5	6.0	32.0
179	Ti-6Al-1.5Mo-0.5V-0.05 O ₂	None	--	--	115.2	120.6	14.0	24.0 ^(e)
		70	91.0	0.155	114.6	121.8	5.0	21.0

(a) Air exposures.

(b) Surfaces as creep exposed.

(c) 0.2 percent offset yield stress.

(d) Percent elongation in 1 inch.

(e) Average tensile properties are given (re Table 4).

The creep data, also given in Table 5, show that although the short-term, 600 F creep exposure is not particularly severe, appreciable plastic strain was obtained. The moderately low aluminum content alpha-beta alloys are not noted for exceptional creep strength.

Aqueous Stress-Corrosion Tests

The single-edge notched, precracked, cantilever test⁽²⁾ was used to determine the fracture toughness and aqueous stress-corrosion susceptibility (3.5 percent NaCl) of the experimental alloys. The same procedure was followed as that described in previous reports⁽¹⁾. Dimensions of the 1/8- and 1/4-inch-thick test specimens were generally as shown in Figure 2. Special tests were conducted using side-notched specimens with the geometry depicted in Figure 3, and 1/2-inch-thick specimens of

commercial-grade Ti-4Al-3Mo-1V alloy as shown in Figure 4. The general test procedure for step-loaded tests was to add an initial load, estimated to result in a stress intensity of about 10 ksi $\sqrt{\text{inch}}$ below the stress intensity for failure, and then to apply additional load in increments equivalent to stress-intensity increments of 1 to 2 ksi $\sqrt{\text{inch}}$ at intervals of 2 to 5 minutes until crack propagation and failure occurred. Tests at constant load were also conducted where exposures to the environment were for 6 hours (a few tests were discontinued in shorter times). The data generated in these tests are given in Tables 6, 7, and 8.

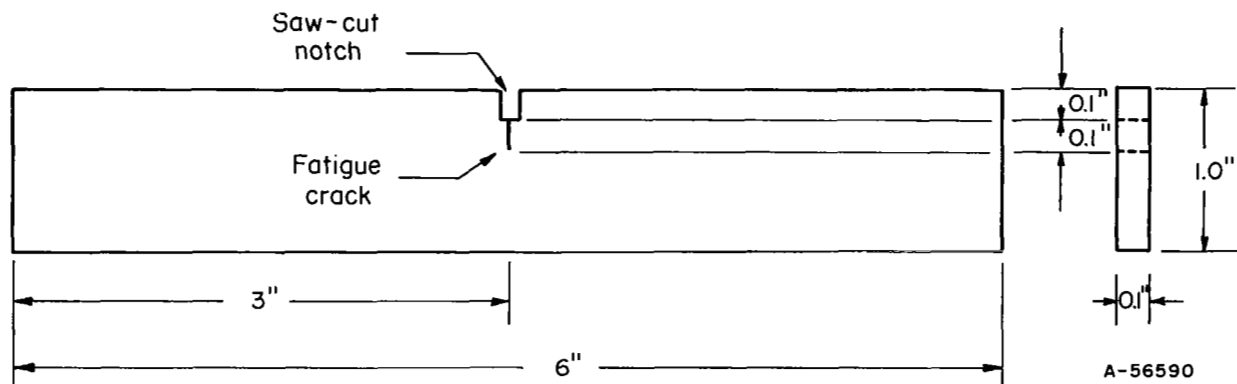


FIGURE 2. GEOMETRY OF PRECRACKED CANTILEVER TEST SPECIMEN

The fracture-toughness values in air and in salt water for 1/8- and 1/4-inch-thick materials are tabulated below. The tabulation reflects an interpretation of the data from Tables 6 and 7 wherein it can be seen that in some cases an exact value was not obtained, or in other cases two somewhat different values were obtained for one condition. Average values are tabulated for the latter case. The differences between the saltwater toughness values obtained in the incremental- and constant-load tests are to be noted as well as the differences obtained for materials of different thickness.

Nominal Composition, weight percent	Stress Intensity, ksi $\sqrt{\text{inch}}$					
	1/8-Inch Thickness			1/4-Inch Thickness		
	In Air	In Salt Water		In Air	In Salt Water	
		Incremental Loading	Constant Load		Incremental Loading	Constant Load
Ti-5Al-1.5Mo-0.5V-0.1 O	91	88	63	84	56	43
Ti-5.5Al-1.5Mo-0.5V-0.1 O	94	88	68	92	81	58
Ti-6Al-1.5Mo-0.5V-0.05 O	98	93	72	86	64	53
Ti-6Al-1.5Mo-0.5V-0.1 O	94	83	64	82	78	58
Ti-6Al-1.5Mo-0.5V-0.18 O	73	27	26	65	25	22
Ti-6.5Al-1.5Mo-0.5V-0.05 O	87	39	27	67	29	24
Ti-6Al-0.1 O	94	90	55	92	79	35
Ti-6Al-2Mo-0.1 O	90	51	32	73	32	25
Ti-6Al-2V-0.1 O	102	41	34	83	31	26
Ti-6Al-4V-0.1 O	92	89	74	76	66	55

The effect of aluminum content on the stress-corrosion susceptibility of Ti-1.5Mo-0.5 V base alloys is clearly evident when the above and prior⁽¹⁾ data are plotted as in Figure 5. In this plot of the data for the 1/8-inch-thick specimen, the air toughness

TABLE 6. FRACTURE-TOUGHNESS DATA OBTAINED FOR 0.125-INCH-THICK SPECIMENS IN AIR AND 3.5 PERCENT NaCl SOLUTION

Alloy	Composition, weight percent	Environment	Loading Method	Stress Intensity, ksi $\sqrt{\text{inch}}$	Total Exposure Time, minutes	Remarks
177	Ti-5Al-1.5Mo-0.5V-0.1 O ₂	Air	Step	90.9	29	Failed
		Salt water	Step	88.5	45	Failed
		Salt water	Step	87.1	28	Failed
		Salt water	Constant	84.0	0.5	Failed
		Salt water	Constant	80.0	0.5	Failed
		Salt water	Constant	66.0	208	Failed
178	Ti-5.5Al-1.5Mo-0.5V-0.1 O ₂	Air	Step	94.3	30	Failed
		Salt water	Step	85.9	43	Failed
		Salt water	Step	90.6	32	Failed
		Salt water	Constant	86.0	31	Failed
		Salt water	Constant	82.0	0.5	Failed
		Salt water	Constant	65.0	360	No failure
179	Ti-6Al-1.5Mo-0.5V-0.05 O ₂	Salt water	Constant ^(a)	72.0	1	Failed
		Air	Step	97.9	34	Failed
		Salt water	Step	93.1	32	Failed
		Salt water	Constant	89.0	~1	Failed
		Salt water	Constant	84.0	0.5	Failed
		Salt water	Constant	79.0	177	Failed
180	Ti-6Al-1.5Mo-0.5V-0.1 O ₂	Salt water	Constant	70.0	360	No failure
		Salt water	Constant ^(a)	75.0	2	Failed
		Air	Step	94.5	27	Failed
		Salt water	Step	75.7	24	Failed
		Salt water	Step	91.0	42	Failed
		Salt water	Constant	73.0	1	Failed
181	Ti-6Al-1.5Mo-0.5V-0.18 O ₂	Salt water	Constant	68.0	214	Failed
		Salt water	Constant	60.0	360	No failure
		Air	Step	72.6	18	Failed
		Salt water	Step	33.8	1	Failed
		Salt water	Step	27.1	10	Failed
		Salt water	Constant	27.0	75	Failed
182	Ti-6.5Al-1.5Mo-0.5V-0.05 O ₂	Salt water	Constant	24.0	360	No failure
		Salt water	Constant	25.5	360	No failure
		Air	Step	86.8	26	Failed
		Salt water	Step	38.7	6	Failed
		Salt water	Constant	35.0	37	Failed
		Salt water	Constant	34.0	33	Failed
183	Ti-6Al-0.1 O ₂	Salt water	Constant	29.0	152	Failed
		Salt water	Constant	25.0	360	No failure
		Air	Step	94.1	22	Failed
		Salt water	Step	89.5	34	Failed
		Salt water	Constant	85.0	1.25	Failed
		Salt water	Constant	80.0	0.5	Failed
		Salt water	Constant	70.0	1.5	Failed
		Salt water	Constant	60.0	5	Failed

TABLE 6. (Continued)

Alloy	Composition, weight percent	Environment	Loading Method	Stress Intensity, ksi $\sqrt{\text{inch}}$	Total Exposure Time, minutes	Remarks
184	Ti-6Al-2Mo-0.1 O ₂	Air	Step	89.6	24	Failed
		Salt water	Step	51.2	12	Failed
		Salt water	Constant	48.0	1.75	Failed
		Salt water	Constant	43.0	2	Failed
		Salt water	Constant	38.0	12	Failed
		Salt water	Constant	30.0	360	No failure
		Salt water	Constant ^(a)	35.0	37	Failed
185	Ti-6Al-2V-0.1 O ₂	Air	Step	102.3	32	Failed
		Salt water	Step	41.1	11	Failed
		Salt water	Constant	36.0	18	Failed
		Salt water	Constant	35.0	5	Failed
		Salt water	Constant	33.0	360	No failure
		Salt water	Constant	30.0	360	No failure
186	Ti-6Al-4V-0.1 O ₂	Air	Step	92.1	28	Failed
		Salt water	Step	88.8	34	Failed
		Salt water	Constant	83.0	170	Failed
		Salt water	Constant	80.0	177	Failed
		Salt water	Constant	66.0	360	No failure
		Salt water	Constant ^(a)	80.0	66	Failed
		Salt water	Constant	73.0	360	No failure
		Salt water	Constant ^(a)	76.0	18	Failed

(a) Rerun of above specimen at higher stress intensity.

TABLE 7. FRACTURE-TOUGHNESS DATA OBTAINED FOR 0.250-INCH-THICK SPECIMEN IN AIR AND 3.5 PERCENT NaCl SOLUTION

Alloy	Composition, weight percent	Environment	Loading Method	Stress Intensity, ksi $\sqrt{\text{inch}}$	Total Exposure Time, minutes	Remarks
177	Ti-5Al-1.5Mo-0.5V-0.1 O ₂	Air	Step	83.6	42	Failed
		Salt water	Step	63.9	22	Failed
		Salt water	Step	56.0	45	Failed
		Salt water	Constant	40.0	360	No failure
		Salt water	Constant ^(a)	46.0	113	Failed
178	Ti-5.5Al-1.5Mo-0.5V-0.1 O ₂	Air	Step	92.4	76	Failed
		Salt water	Step	85.0	60	Failed
		Salt water	Step	77.7	58	Failed
		Salt water	Constant	60.0	350	Failed
179	Ti-6Al-1.5Mo-0.5V-0.055 O ₂	Air	Step	86.2	64	Failed
		Salt water	Step	63.8	45	Failed
		Salt water	Constant	56.0	21.5	Failed
		Salt water	Constant	50.0	360	No failure
180	Ti-6Al-1.5Mo-0.5V-0.1 O ₂	Air	Step	82.3	64	Failed
		Salt water	Step	78.5	73	Failed
		Salt water	Step	77.1	64	Failed
		Salt water	Constant	50.0	360	No failure
		Salt water	Constant ^(a)	56.0	180	No failure
181	Ti-6Al-1.5Mo-0.5V-0.175 O ₂	Air	Step	64.9	34	Failed
		Salt water	Step	25.2	19	Failed
		Salt water	Constant	24.0	5	Failed
		Salt water	Constant	20.0	360	No failure
182	Ti-6.5Al-1.5Mo-0.5V-0.055 O ₂	Air	Step	67.3	46	Failed
		Salt water	Step	29.1	10	Failed
		Salt water	Constant	25.0	15	Failed
		Salt water	Constant	20.0	360	No failure
		Salt water	Constant ^(a)	23.0	180	No failure
183	Ti-6Al-0.1 O ₂	Air	Step	92.2	64	Failed
		Salt water	Step	79.2	61	Failed
		Salt water	Constant	60.0	1.5	Failed
		Salt water	Constant	40.0	3	Failed
184	Ti-6Al-2Mo-0.1 O ₂	Air	Step	73.0	50	Failed
		Salt water	Step	31.9	14	Failed
		Salt water	Constant	30.0	6	Failed
		Salt water	Constant	24.0	360	No failure
		Salt water	Constant ^(a)	27.0	7	Failed
185	Ti-6Al-2V-0.1 O ₂	Air	Step	83.4	66	Failed
		Salt water	Step	31.3	19	Failed
		Salt water	Constant	28.0	6	Failed
		Salt water	Constant	24.0	360	No failure
		Salt water	Constant ^(a)	26.0	180	No failure
186	Ti-6Al-4V-0.1 O ₂	Air	Step	76.2	52	Failed
		Salt water	Step	66.3	58	Failed
		Salt water	Constant	58.0	2.5	Failed
		Salt water	Constant	50.0	360	No failure
		Salt water	Constant ^(a)	54.0	180	No failure

(a) Rerun of above specimen at higher stress intensity.

TABLE 8. FRACTURE-TOUGHNESS DATA OBTAINED FOR 0.250-INCH-THICK SIDE-NOTCHED SPECIMEN IN 3.5 PERCENT NaCl SOLUTION

Alloy	Composition, weight percent	Loading Method	Stress Intensity, ksi $\sqrt{\text{inch}}$	Total Exposure Time, minutes	Remarks
177	Ti-5Al-1.5Mo-0.5V-0.1 O ₂	Step	64.4	18	Failed
		Constant	40.0	<1	Failed
		Constant	35.0	360	No failure
		Constant	30.0	360	No failure
178	Ti-5.5Al-1.5Mo-0.5V-0.1 O ₂	Constant	68.0	123	Failed
		Constant	60.0	360	No failure
		Constant ^(a)	64.0	56	Failed
		Constant	45.0	360	No failure
		Step ^(b)	74.3	55	Failed
179	Ti-6Al-1.5Mo-0.5V-0.055 O ₂	Step	90.5	54	Failed
		Constant	50.0	360	No failure
		Constant ^(a)	55.0	180	No failure
		Constant	45.0	360	No failure
180	Ti-6Al-1.5Mo-0.5V-0.1 O ₂	Constant	40.0	360	No failure
		Constant ^(a)	46.0	180	No failure
		Constant ^(c)	50.0	88	Failed
		Constant	37.0	360	No failure
		Step ^(b)	63.1	42	Failed
		Constant	35.0	360	No failure
		Step ^(b)	39.1	9	Failed
183	Ti-6Al-0.1 O ₂	Step	52.0	28	Failed
		Constant	35.0	360	No failure
		Constant	30.0	360	No failure
		Constant	40.0	360	No failure
		Constant ^(a)	45.0	360	No failure
		Constant ^(a)	50.0	360	No failure
41	Ti-4Al-3Mo-1V (Commercial) ^(d)	Step ^(e, f)	84.1	129	Failed
		Step ^(f)	74.5	93	Failed
		Constant ^(f)	70.0	360	No failure
		Step ^(f, g)	72.1	1	Failed
		Step ^(h)	73.3	92	Failed
		Constant ^(h)	65.0	360	No failure
		Constant ^(h)	68.0	6	Failed

(a) Rerun of above specimen at higher stress intensity.

(b) Above specimen step loaded to failure after 360 minutes' exposure under constant load.

(c) Second rerun of above specimen at higher stress intensity.

(d) One-half-inch-thick specimens.

(e) Test in air.

(f) No side notch.

(g) Prior sample step loaded to failure after 360 minutes' exposure under constant load.

(h) Rerun of prior sample at higher stress intensity.

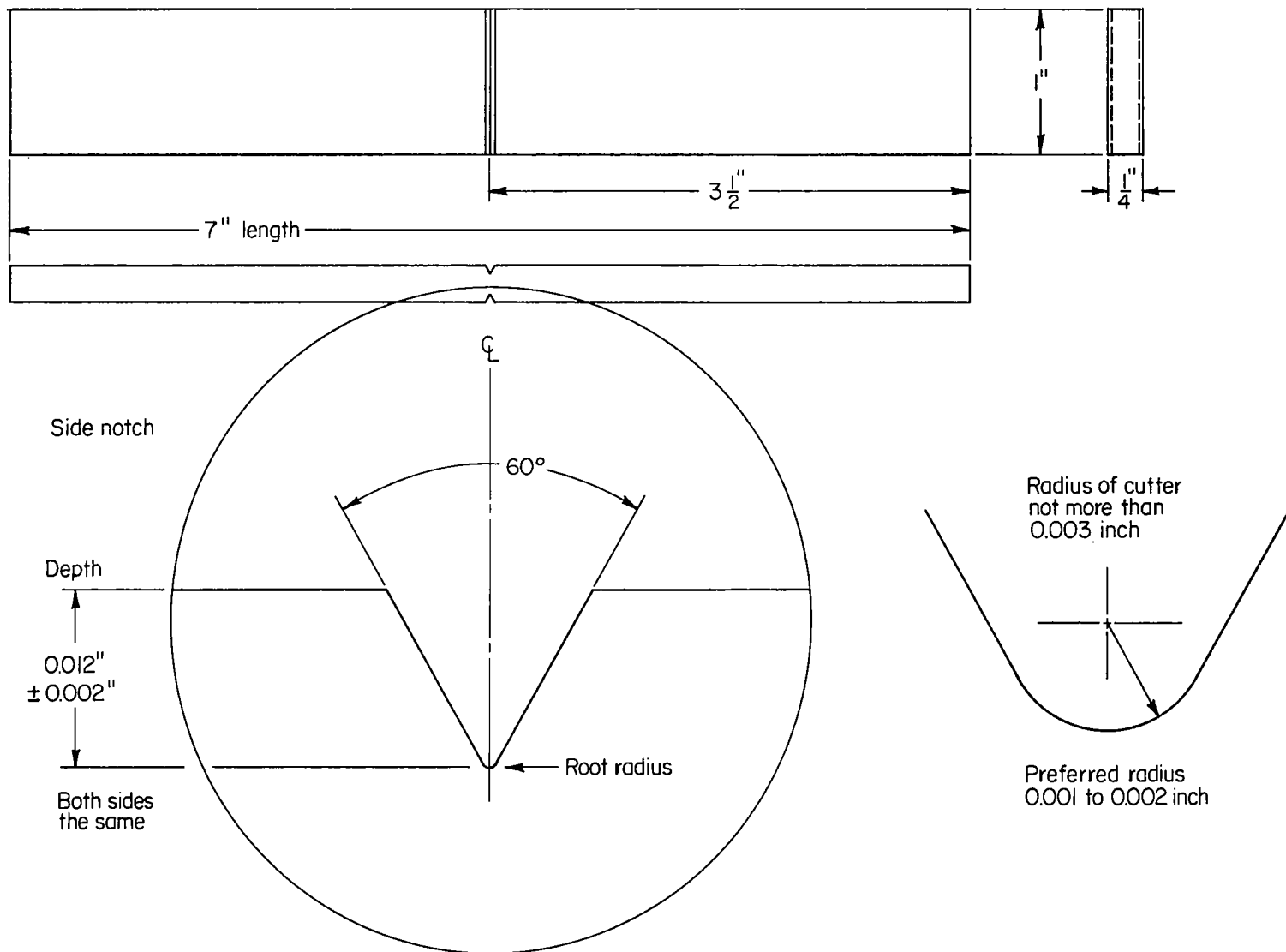


FIGURE 3. GEOMETRY OF SIDE-NOTCHED SPECIMENS (BOTH SIDES NOTCHED)

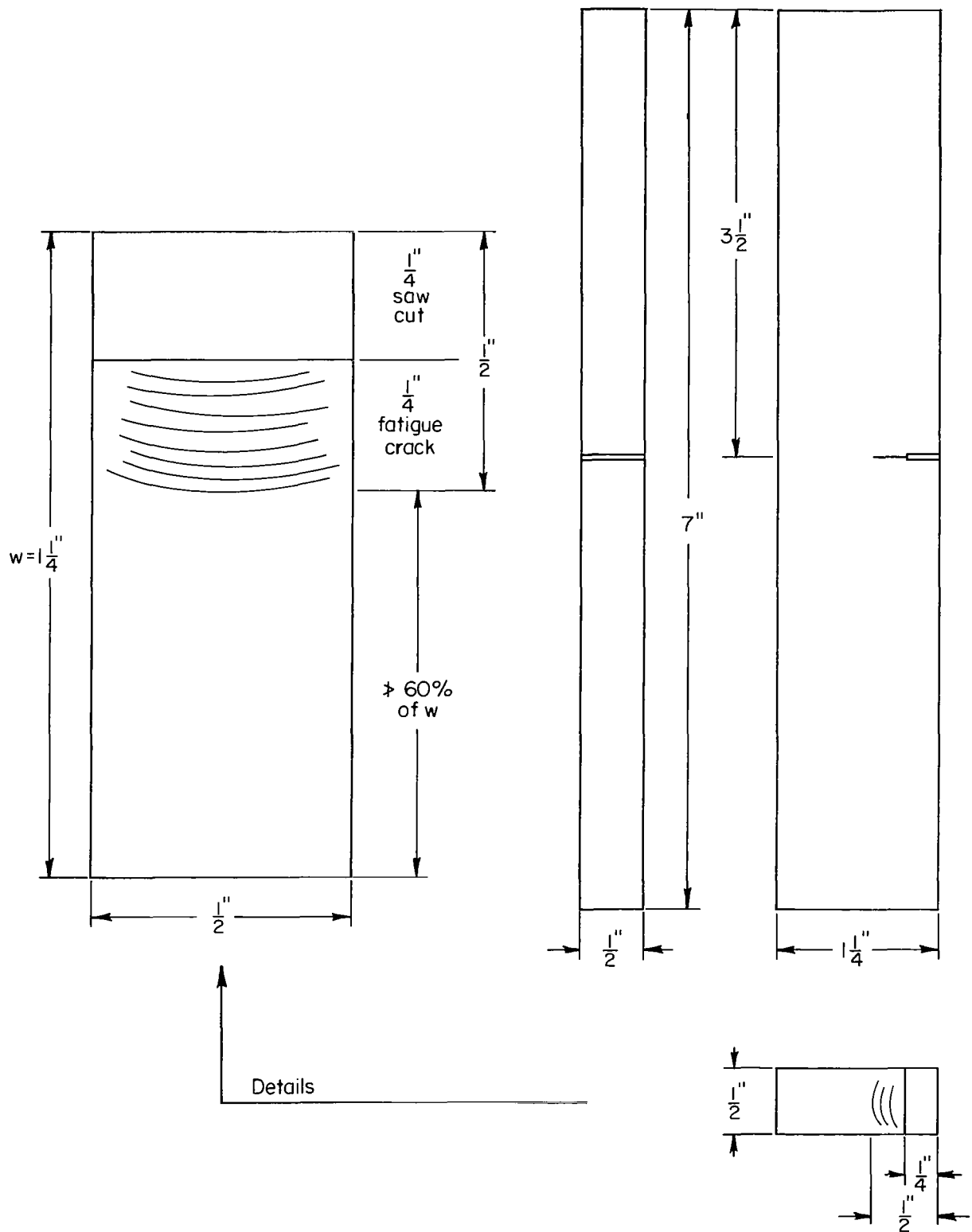


FIGURE 4. GEOMETRY OF 1/2-INCH-THICK SPECIMENS, CANTILEVER NOTCH BEND TEST

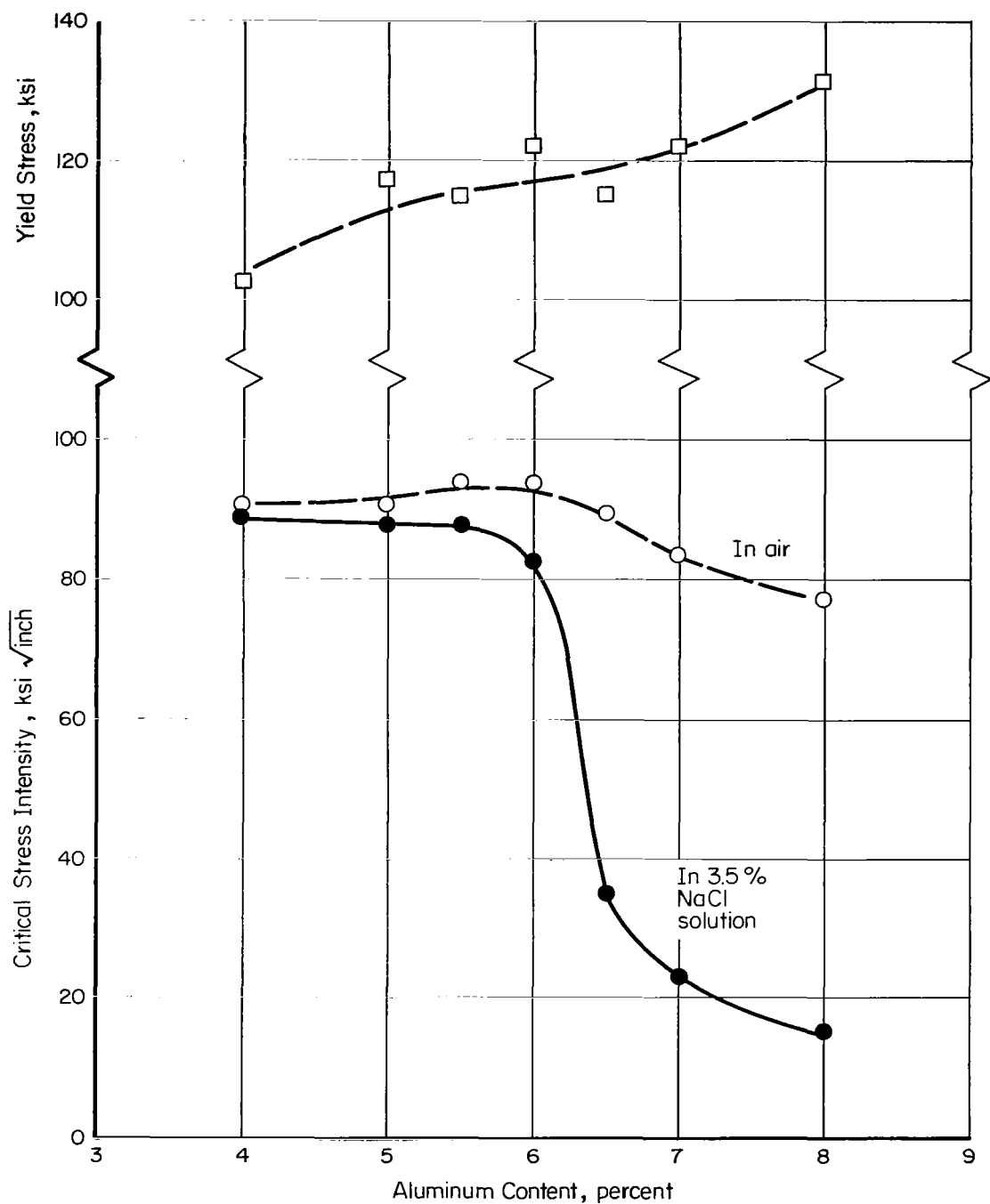


FIGURE 5. EFFECT OF ALUMINUM CONTENT ON THE STRENGTH, TOUGHNESS, AND STRESS-CORROSION SUSCEPTIBILITY OF Ti-1.5Mo-0.5V-BASE ALLOYS (NOMINALLY 1000 PPM OXYGEN)

Data are for 1/8-inch-thick specimens; incremental load tests.

is seen to decrease slightly at aluminum contents above 6 percent, while yield stress increases with increasing aluminum content. The most striking feature of the diagram however is the abrupt degradation of salt-water toughness for alloys having more than 6 percent aluminum. Optimum combinations of strength, toughness, and comparative immunity to salt-water cracking appear to be available in the material containing 5.5 to 6 percent aluminum.

The effect of the total alpha-stabilizer content, that is aluminum plus oxygen, on the stress-corrosion susceptibility of the above type of compositions is illustrated in Figure 6. This plot of the data for the incrementally loaded 1/8-inch-thick specimen shows the detrimental effect of increasing oxygen content on the salt-water toughness. A very low oxygen content does benefit a susceptible base, such as a Ti-7Al base. However, the oxygen level required to result in a major benefit is lower than that which is practical commercially. On the other hand, low-to-medium oxygen contents of practical commercial range in the Ti-6Al base permit a large degree of immunity, with immunity decreasing as oxygen content is increased.

The effects of a beta-stabilizer content on the strength-toughness-susceptibility relationships in a titanium-aluminum base that is marginally susceptible to salt-water stress corrosion depend upon the amount and kind of beta-stabilizer content. Such effects may be compositionally-dependent – that is, the result of the portion of the beta-stabilizer addition in solution in the alpha phase – or microstructurally-dependent, owing to differences in amount and distribution of the beta phase. Figure 7 shows such relationships for the combinations of beta stabilizers augmenting the Ti-6Al~0.1 O₂ base. Data for incrementally loaded 1/8-inch-thick specimens are shown. In this case it can be seen that an initial small beta addition apparently decreases salt-water toughness, while air toughness remains essentially unchanged, and strength is increased. These effects are attributed largely to the soluble portion of the beta addition. An increase in beta-stabilizer addition, that is, from 2 percent vanadium to 4 percent vanadium, resulted in improvement in salt-water toughness without a change in strength. This might be attributed to the increased amount of beta phase. At the 2 percent level, the 1.5Mo-0.5V percent beta-stabilizer combination appears to offer more favorable combinations of strength and toughness than either 2 percent vanadium or 2 percent molybdenum used singly, although a strength advantage is shown for the Ti-6Al-2Mo alloy. None of the alloys with 2 percent beta-stabilizer content are as immune to salt-water stress corrosion as the Ti-6Al-4V composition however.

The effect of specimen thickness in the toughness test is of major importance in any attempt to determine valid fracture-toughness values. For a single-edge-cracked cantilever specimen, a valid plane-strain fracture toughness is measured only when the thickness is greater than $(K/Y)^{2(3)}$. Since the preceding discussion concerns data for 1/8-inch thick specimens, it is recognized that the comparisons of alloying effects are in many cases qualitative. Specimens 1/4 inch thick were also tested in an attempt to gain insight into the effect of thickness as it might be related to compositional effects. In addition, side-notched 1/4-inch-thick specimens were tested in a further attempt to gain a pure plane-strain condition for some of the low-strength materials. Also, 1/2-inch thick Ti-4Al-3Mo-1V specimens, with and without a side notch, were tested. The data obtained in these tests are given in Table 8.

Selected data showing the effect of sample thickness on air and salt-water toughness are shown below.

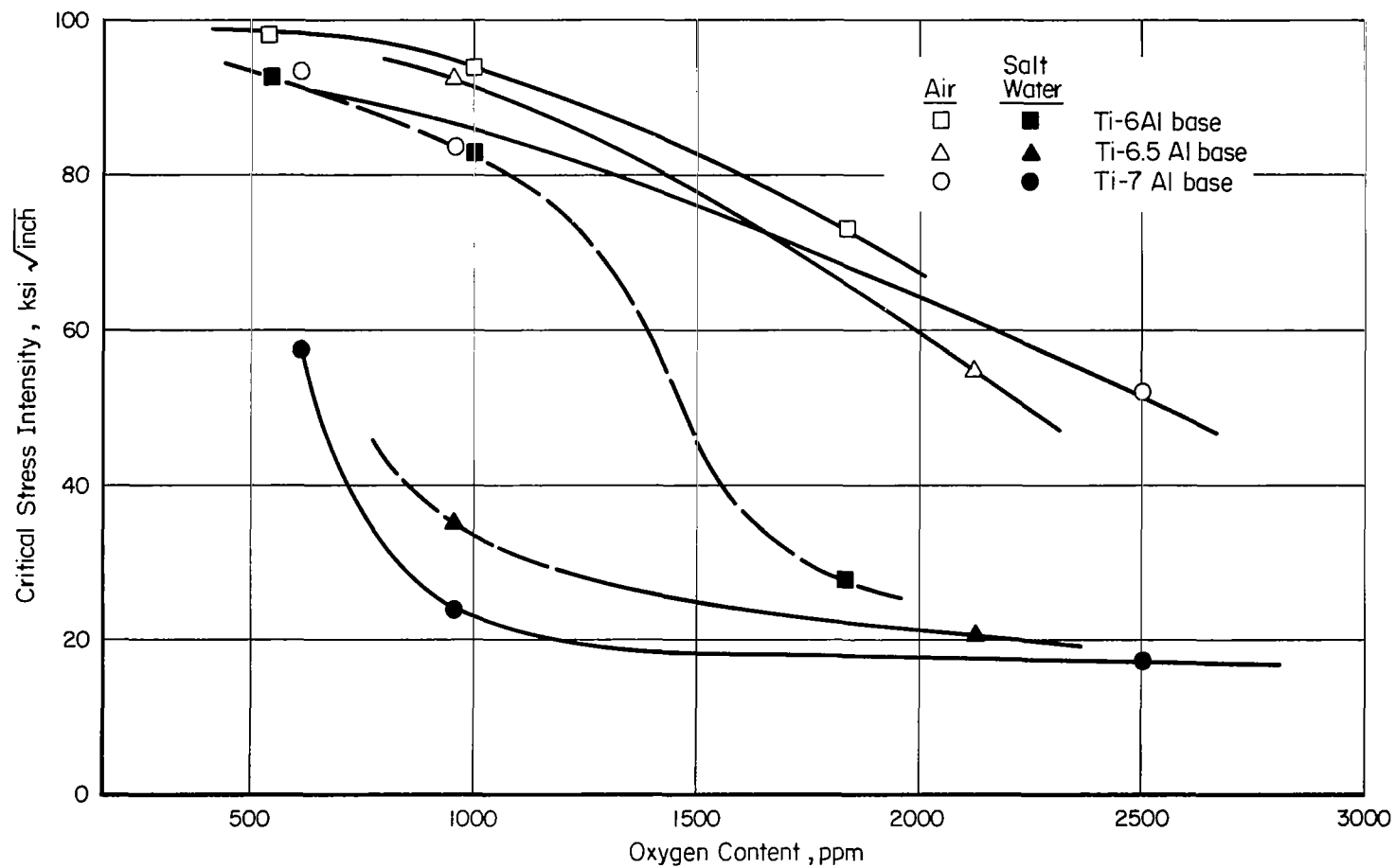


FIGURE 6. EFFECT OF OXYGEN CONTENT ON THE TOUGHNESS AND STRESS-CORROSION SUSCEPTIBILITY OF Ti-(6, 6.5, 7)Al-1.5Mo-0.5V ALLOYS

Data are for 1/8-inch-thick specimens; incremental load tests.

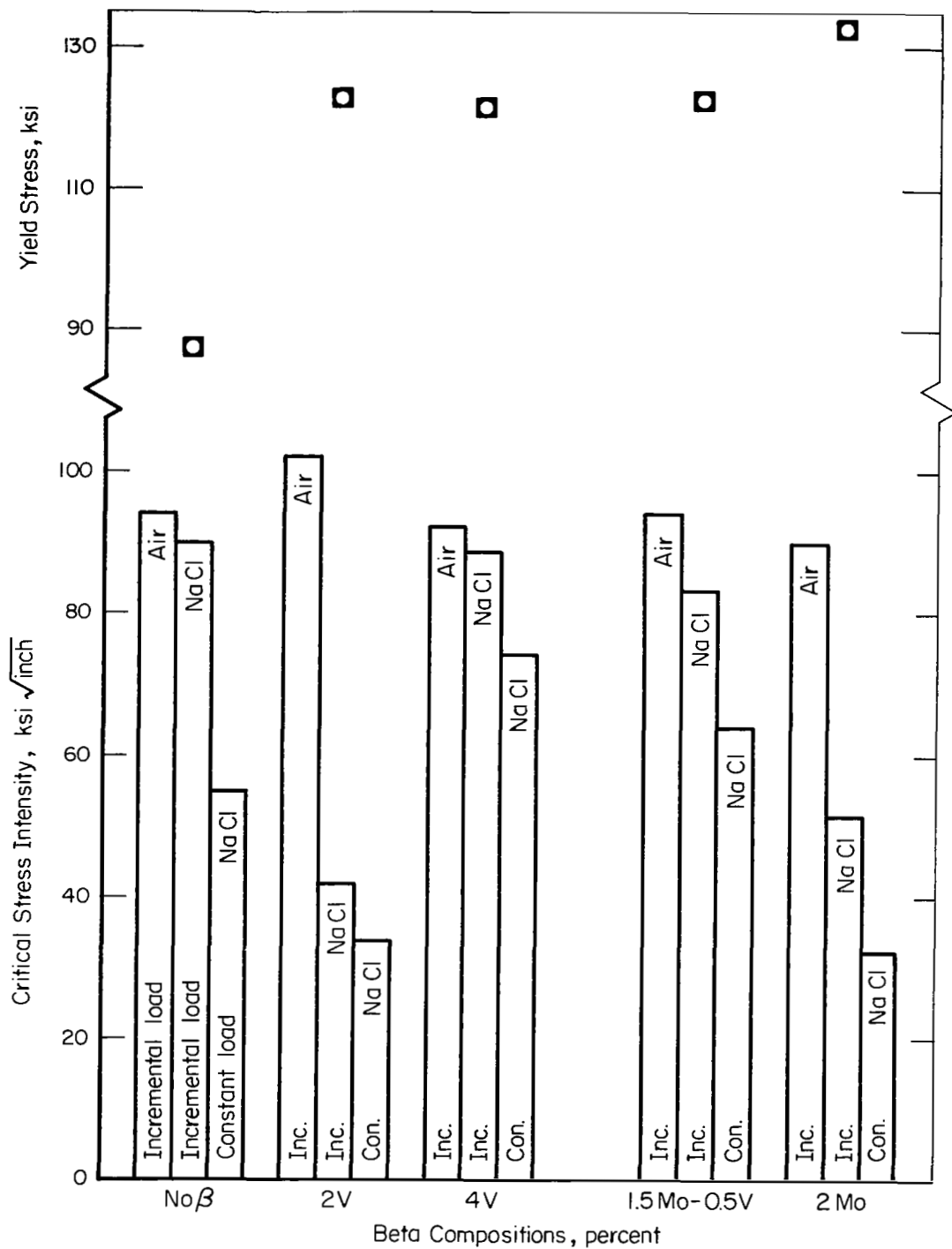


FIGURE 7. EFFECT OF BETA STABILIZER AMOUNT AND KIND ON YIELD STRENGTH, TOUGHNESS, AND STRESS-CORROSION SUSCEPTIBILITY OF Ti-6Al BASE ALLOYS (1000 PPM O₂)

Data are for 1/8-inch-thick specimens.

Nominal Composition, weight percent	Sample Thickness, inch	Stress Intensity, ksi $\sqrt{\text{inch}}$		
		Air Value	Salt-Water Values	
			Incremental	Constant
Ti-4Al-3Mo-1V	0.125	93	90	86
	0.500	84	74	71
	0.500 SN*	--	73	66
Ti-5Al-1.5Mo-0.5V	0.125	91	88	63
	0.250	84	56	43
	0.250 SN	--	64	37
Ti-5.5Al-1.5Mo-0.5V	0.125	94	88	68
	0.250	92	81	58
	0.250 SN	--	74	62
Ti-6Al-1.5Mo-0.5V	0.125	94	83	64
	0.250	82	78	58
	0.250 SN	--	63	48
Ti-6Al-4V	0.125	92	89	74
	0.250	76	66	55

*SN = side notched.

The data show that although absolute toughness values are lower as the state of stress approaches more closely a plane-strain condition, the composition effects indicated in tests of thinner specimens are not much changed. Except for the Ti-5Al-1.5Mo-0.5V alloy, the thick sample data show that marginal aluminum content for stress-corrosion immunity is about 6 percent. On the other hand, fairly low salt-water toughness values were obtained for the thicker samples of Ti-5Al-1.5Mo-0.5V alloy. The low values for this alloy are not understood at this time in terms of the higher salt-water toughness values obtained in equivalent tests for Ti-5.5Al- and Ti-6Al-base alloys. It is apparent that there is a thickness effect however, since even the nonsusceptible Ti-4Al-3Mo-1V composition has lowered salt water toughness values when thick samples are tested. It is obvious that should a prediction of a particular alloy's behavior be desired on an engineering basis, correct thickness samples would need to be evaluated.

MECHANISMS OF STRESS-CORROSION CRACKING

Aqueous Environments

Introduction

During the past year a detailed metallographic study has been made of the morphology of stress-corrosion cracks and of the distribution of slip within the crack-tip plastic zone. These results, the results of earlier work on this program⁽¹⁾, and the results of other workers⁽⁴⁾, have been used to formulate a phenomenological model for aqueous stress-corrosion cracking of titanium alloys. In addition, the crack-velocity data reported earlier⁽¹⁾ have been reanalyzed in terms of an analytic

relationship between crack velocity and applied stress intensity. These data will be used to test quantitative models when they are available.

Experimental

Material. The specimen material used throughout this investigation was commercial Ti-8Al-1Mo-1V. The manufacturer's chemical analysis was as follows (weight percent): 7.9 Al, 1.0 Mo, 1.0 V, 0.06 Fe, 0.02 C, 0.088 O, 0.0078 H. The 1-inch-thick starting material was reduced to approximately 0.25 inch thick by hot rolling, (rolling temperature = 1900 to 1750 F). After grit blasting and surface grinding, 2 by 8-inch transverse specimen blanks were cut. The blanks were annealed as follows:

1/2 hour at 1775 F (in argon), furnace cool to 1200 F (in argon)

1/2 hour at 1200 F (in argon), air cool

3 hours at 1200 F in vacuum (5×10^{-5} torr), argon quench.

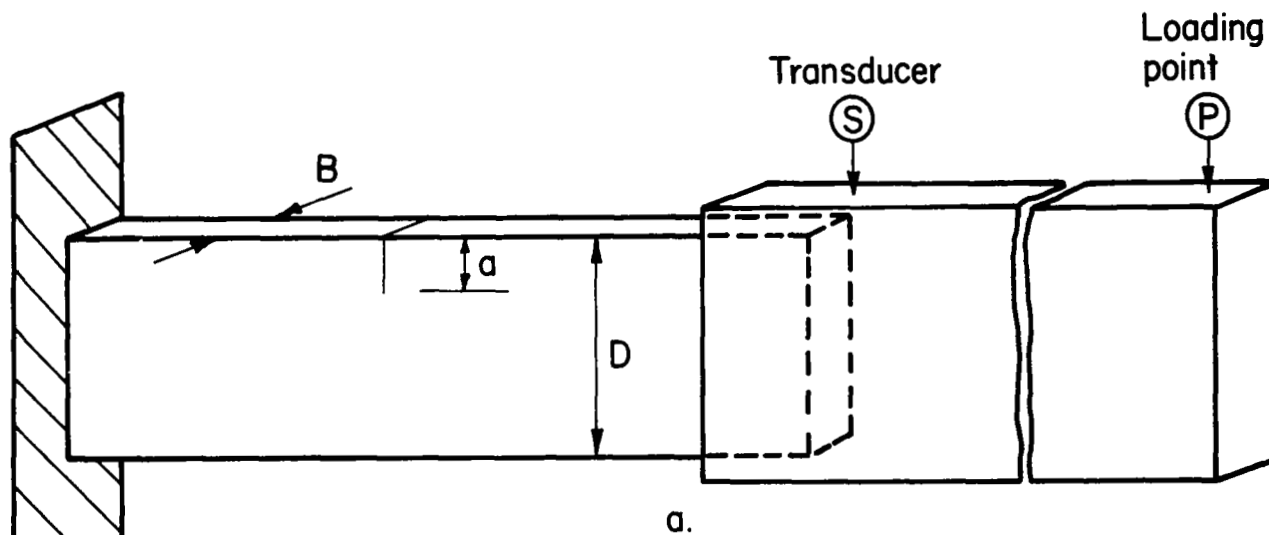
This thermomechanical treatment resulted in an equiaxed alpha grain structure with an average grain size of 10 microns (see Figure 14). The mechanical properties were as follows: 0.2 percent offset yield stress ($\dot{\epsilon} = 2.0 \text{ min}^{-1}$), $Y = 150$ ksi, percent reduction in area = 13.1.

Specimen Geometry and Testing Procedure. Precracked, single edge-notched cantilever specimens were prepared from the annealed blanks. A 0.1-inch-deep saw cut was located in the edge of each specimen at the midpoint of the long dimension, and a fatigue crack was propagated from the root of the notch to produce a total crack length (saw cut plus fatigue crack) of 0.2 to 0.3 inch. The fatigue crack was propagated in air by loading the specimen in three-point bending with the notch on the tension side of the beam.

The cantilever loading arrangement is shown schematically in Figure 8. The specimen was gripped rigidly at one end and loaded via a lever arm fixed on the other end. The load was increased incrementally from zero until subcritical cracking began. Thereafter the crack was allowed to propagate at constant load. A plastic bottle was fitted over the middle portion of the specimen to contain the appropriate test environment. The standard test environment was an aqueous solution containing 3.5 weight percent NaCl (2.1×10^3 ppmw), at room temperature and pH = 6.5. The effects of environment temperature were investigated over the range 32 to 200 F. This was accomplished by surrounding the plastic bottle with various constant-temperature baths. The effects of environment chemistry were investigated by varying the chloride-ion concentration $[\text{Cl}^-]$ over the range $0.1 - 2.1 \times 10^3$ ppmw. The environment containing the lowest chloride-ion concentration was doubly distilled, deionized water ($[\text{Cl}^-] = 0.1$ ppmw).

The specimen geometry and loading arrangement was such that the plane subjected to the maximum tensile stress (which coincided with the plane of the crack) was the plane containing the rolling direction and the normal to the surface of the rolled plate. The crack propagation direction was parallel to the rolling direction (Figure 8).

During each test the instantaneous crack length was measured by means of a transducer mounted on the lever arm, and connected via a linear-variable-differential



$$K_I = \frac{4.12 M \sqrt{\alpha^{-3} - \alpha^3}}{BD^{3/2}}$$

$$\alpha = 1 - a/D$$

$$B = 0.25 \text{ in.}$$

$$D = 2.0 \text{ in.}$$

$$a_0 \approx 0.3 \text{ in.}$$

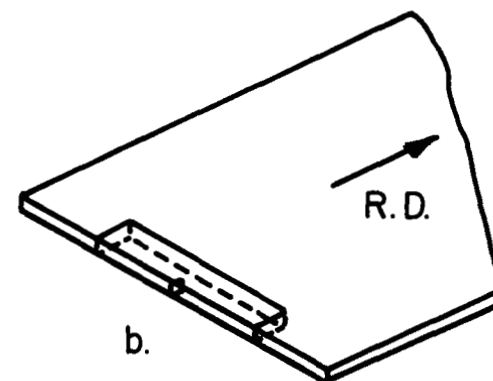


FIGURE 8. SPECIMEN GEOMETRY AND LOADING ARRANGEMENT

transformer (LVDT) to a pen recorder. The transducer continuously monitored the lever-arm deflection, and these data could be converted to measurements of crack length after calibration of the apparatus. The apparatus was calibrated by placing a specimen containing a precrack (saw cut and fatigue crack) of known length in position and zeroing the recorder. The specimen was then loaded in air and the LVDT reading was recorded for each load. The specimen was loaded and unloaded several times to verify that the relationship between LVDT reading and load was single-valued for a constant crack length. Next a bottle of salt water was placed around the crack, a load was applied, and the crack was allowed to grow approximately 0.1 inch in length. The salt water was then removed, the specimen washed and dried, and the LVDT-load relationship determined for the new crack length. This procedure was repeated until a family of curves was generated representing the relationship between LVDT reading and load for various crack lengths ranging from 0.30 inch to 1.3 inch (Figure 9). The actual tests were carried out by loading the specimen incrementally until subcritical crack growth began. The crack was then allowed to propagate at constant load until complete fracture occurred. A calibration curve for each test was constructed by drawing a vertical line on the calibration chart (Figure 9) corresponding to the load used during crack propagation, and reading off the LVDT reading as a function of crack length. The LVDT readings which were recorded during the test could then be converted to crack lengths, and the crack velocities calculated from plots of crack length against time. For each test, two checks were made on the accuracy of the calibration curve. The crack lengths before and after the test were measured accurately, and the LVDT readings given by the calibration curve were compared with the actual readings. In most cases these comparisons showed good agreement (within 10 percent). Whenever there was a larger discrepancy, the data were discarded.

The applied stress intensity at the crack tip was calculated using the expression for plane-strain relaxations⁽²⁾:

$$K_I = \frac{4.12 M \sqrt{\alpha^{-3} - \alpha^3}}{BD^{3/2}}, \quad (1)$$

$$\alpha = 1 - a/D, \quad (2)$$

where M is the bending moment at the crack tip, a is crack length, B is specimen thickness, and D is specimen width (Figure 8). The maximum stress intensity at the point of complete fracture, K_{I_x} , in these experiments was $67.4 \text{ ksi}\sqrt{\text{in.}}$ (see Table 11). Taking $B = 0.25 \text{ inch}$, $K = 67.4 \text{ ksi}\sqrt{\text{in.}}$, and $Y = 150 \text{ ksi}$, the criterion for plane-strain relaxations⁽³⁾:

$$B > \left(\frac{K}{Y} \right)^2 \quad (3)$$

is satisfied. Thus, it is valid to use Equation (1) for calculating K_I since plane-strain conditions persisted up to the point of complete fracture.

Metallography. The morphology of the stress-corrosion cracks was investigated by optical microscopy, and by electron microscopy of surface replicas. The specimens used for these studies were polished metallographically and electropolished prior to testing. Subcritical cracking was initiated in the usual way, but the test was interrupted when the crack had reached the desired length. The load was then removed, the specimen was quickly taken from the aqueous environment, washed, and cleaned ultrasonically to remove all traces of salt from the crack. Conventional two-stage carbon replicas were made of the regions where the crack front intersected the electropolished faces.

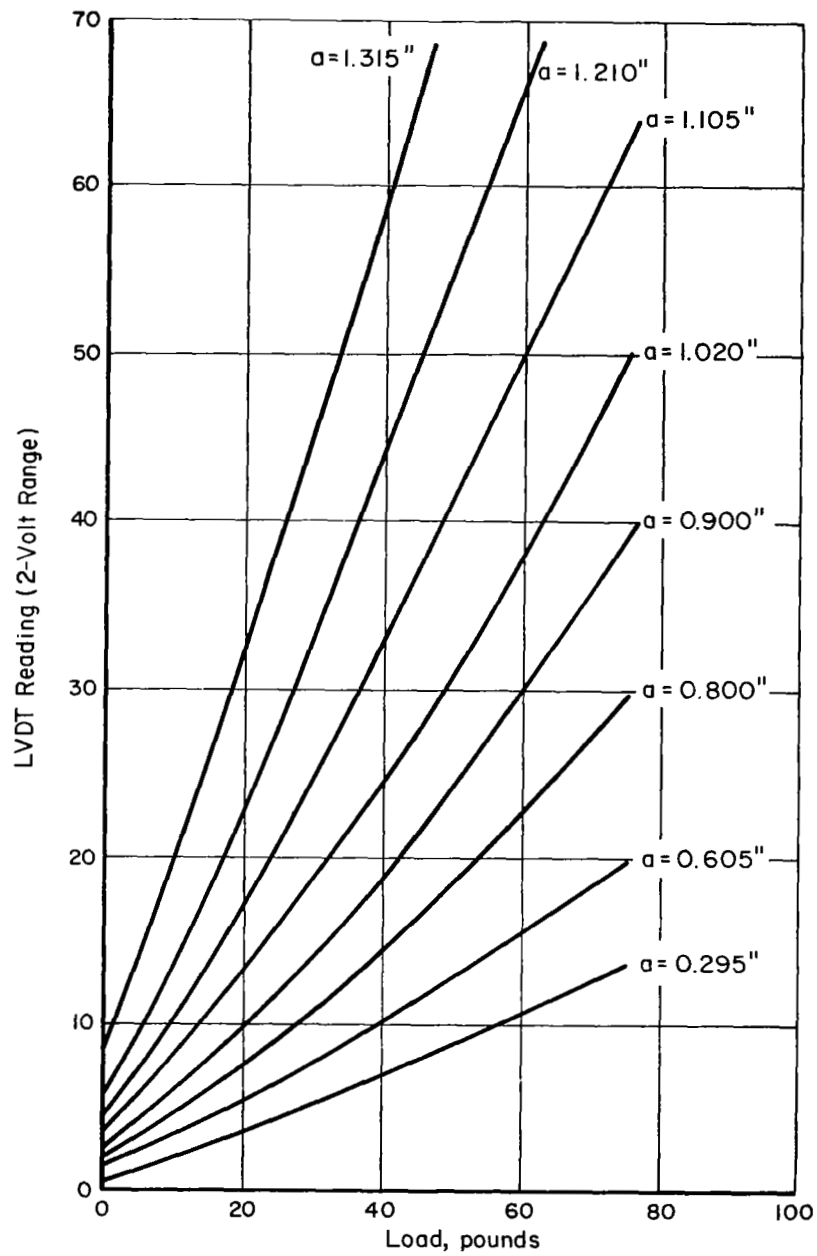


FIGURE 9. CALIBRATION CHART FOR CRACK VELOCITY MEASUREMENTS

The specimen was then etched and the crack tip was examined optically. A three-dimensional picture of the crack was developed by serial sectioning parallel to the side faces of some specimens.

Fractography. The fractured surfaces were examined optically and by scanning electron microscopy. In order to improve the resolution of the scanning electron micrographs, the fracture faces were coated with a thin layer of vapor-deposited gold.

Results

Crack-Velocity Measurements. In a single-edge-notched cantilever test, the stress intensity at the crack tip, K_I , increases continuously as the crack propagates. Thus, for each combination of environmental conditions the relationship between crack velocity and stress intensity could be determined from a single test. All of the results are presented as plots of crack velocity, \dot{a} , against K_I . Typical results for tests performed under standard conditions (room temperature, 3.5 percent NaCl) are shown in Figure 10. Data from two independent tests are shown to illustrate that the results were quite reproducible. (The "data points" are somewhat arbitrary since they were calculated from selected points on the continuous record of LVDT readings.) The curve in Figure 10 shows several fractures which appear to be characteristic of subcritical crack propagation in titanium alloys in aqueous environments:

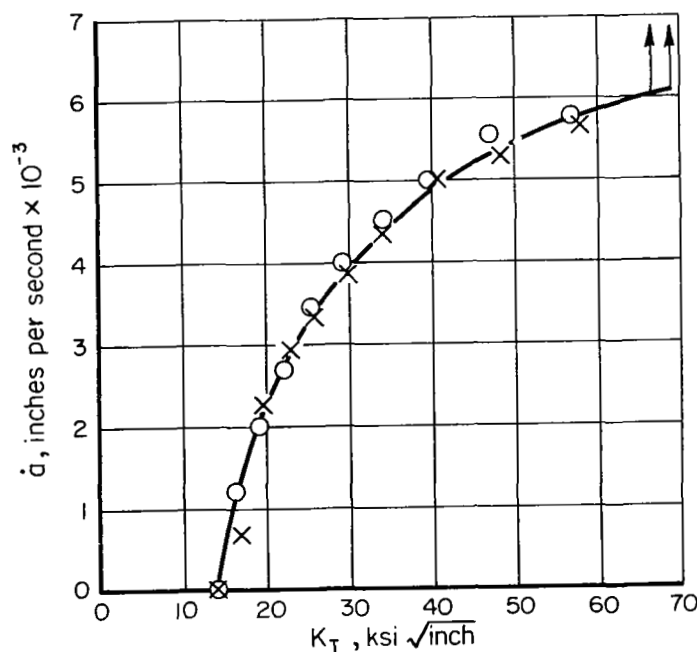


FIGURE 10. SUBCRITICAL-CRACK VELOCITIES FOR Ti-8Al-1Mo-1V, IN 3.5 PERCENT NaCl, AT ROOM TEMPERATURE

- (1) There was a minimum stress intensity, $K_{I_{SCC}}$, which had to be exceeded before subcritical cracking began
- (2) At the onset of subcritical cracking, \dot{a} increased rapidly with increasing K_I , but the dependence of \dot{a} on K_I became less at higher values of K_I when \dot{a} approached a constant value, \dot{a}^0
- (3) Rapid fracture occurred when the stress intensity became equal to the fracture toughness, K_{I_x}

The effects of environment temperature are illustrated by the results given in Figure 11. These data show that:

- (1) The \dot{a} - K_I curves all had the same general shape, but for a given K_I , \dot{a} increased rapidly with increasing temperature.
- (2) At higher temperatures the limiting crack velocity, \dot{a}^0 , was reached at lower values of K_I than it was at lower temperatures.
- (3) There was no significant variation in $K_{I_{SCC}}$ with temperature.
- (4) There was no significant variation in K_{I_x} with temperature.

The effects of chloride-ion concentration are illustrated in Figure 12. These results show that:

- (1) The \dot{a} - K_I curves all had the same general shape, but for a given K_I , \dot{a} increased with increasing $[Cl^-]$.
- (2) The limiting crack velocity, \dot{a}^0 , was reached at lower values of K_I with decreasing $[Cl^-]$.
- (3) $K_{I_{SCC}}$ varied inversely with $[Cl^-]$.
- (4) K_{I_x} decreased slightly with decreasing $[Cl^-]$.

Crack-Tip Morphologies. All of the metallographic studies were made on specimens tested under the standard environmental conditions. Figure 13 illustrates the variation in the morphology of a crack front through the thickness of the specimen. The crack shown in Figure 13 was stopped when its length corresponded to an applied stress intensity of $53 \text{ ksi}\sqrt{\text{in}}$. The various micrographs were taken after serial sectioning parallel to the broad side face of a single specimen. (d refers to the distance from the surface, and the individual micrographs are correctly aligned relative to each other.) It can be seen from Figure 14 that the crack was predominantly transgranular through the alpha grains, and microscopically the crack path often deviated considerably from the average direction of propagation. Furthermore, the crack-tip morphology varied markedly along the crack front (i.e., through the thickness of the specimen). Two distinct morphologies were observed:

- (1) "Ragged" cracks that consisted of straight segments 0.004 to 0.008 inch in length. At the tip of each segment the crack was "wiggly", changing direction from one grain to the next. This type of morphology is illustrated by

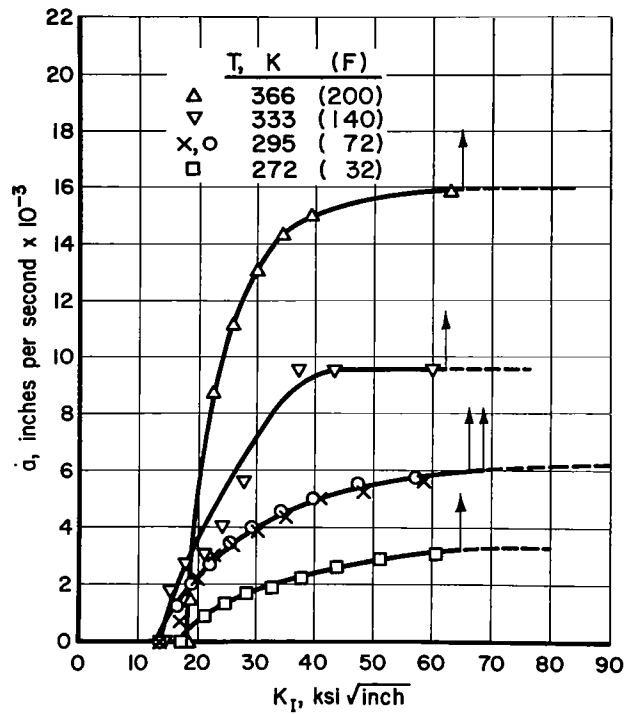


FIGURE 11. EFFECT OF ENVIRONMENT TEMPERATURE ON SUBCRITICAL-CRACK VELOCITIES

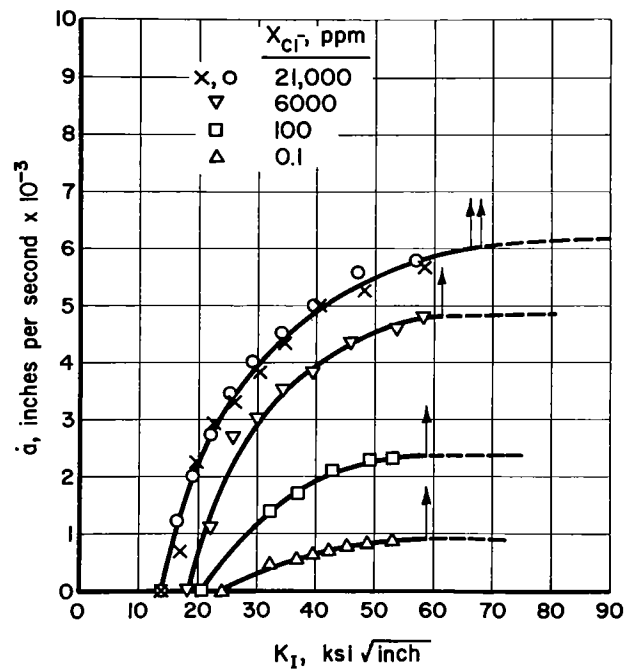
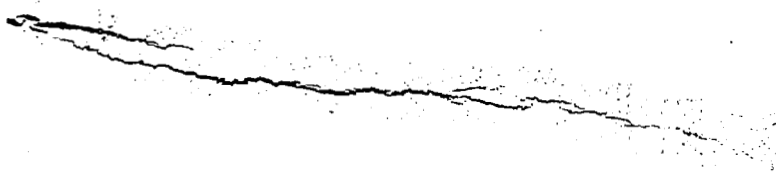
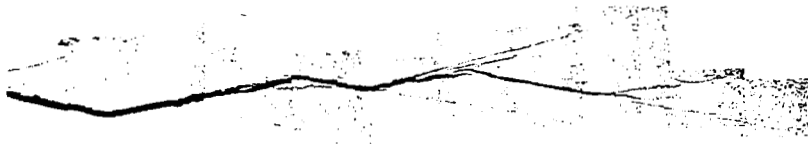


FIGURE 12. EFFECT OF BULK CHLORIDE-ION CONCENTRATION ON SUBCRITICAL-CRACK VELOCITIES



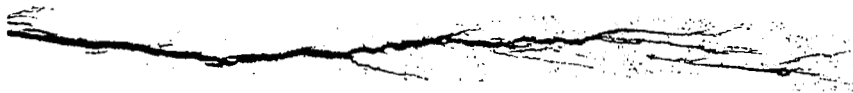
$d=0.0015$ in.

a



$d=0.0075$

b



$d=0.0100$

c



$d=0.1395$

d



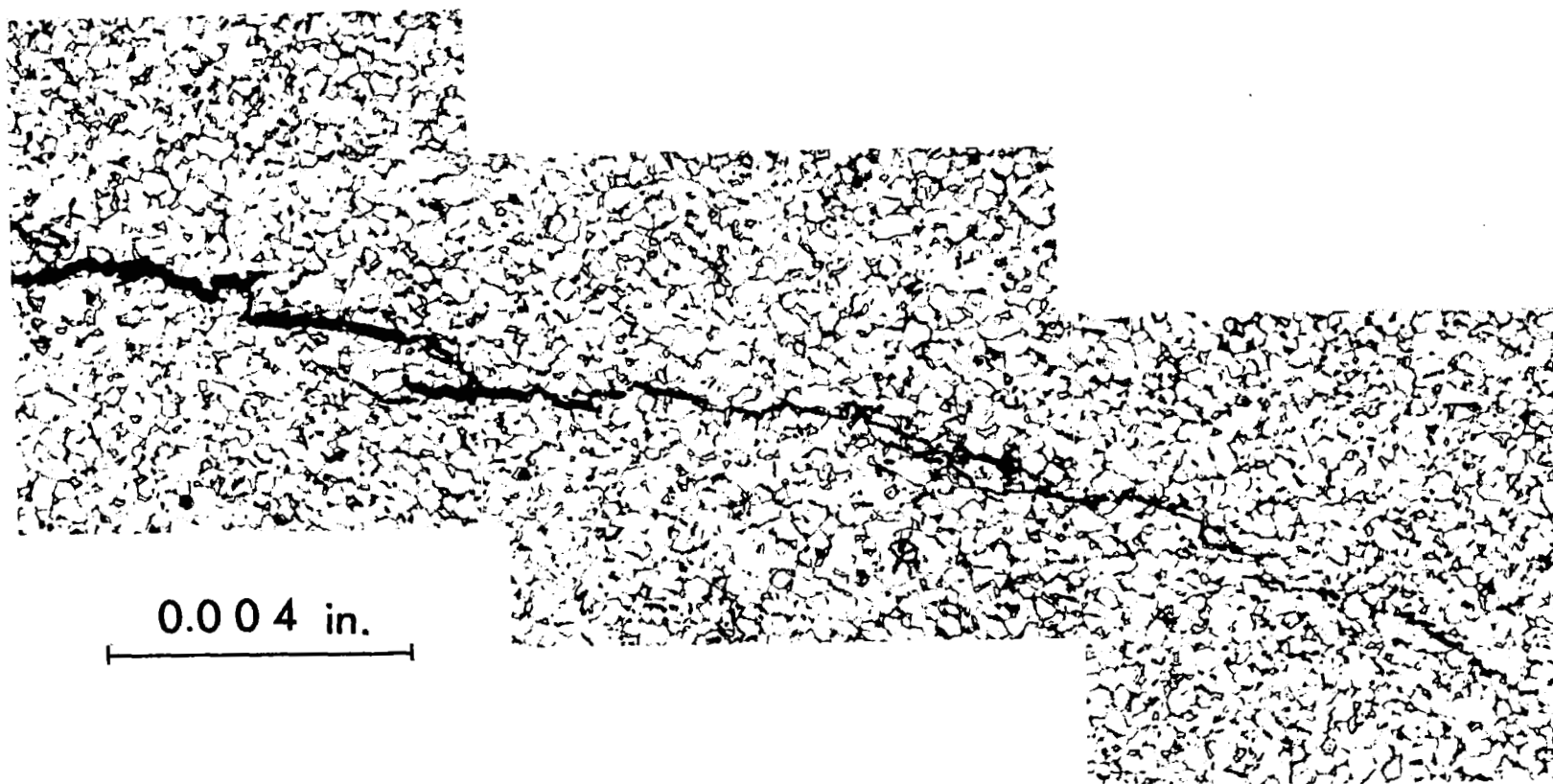
$d=0.1420$

e

0.02 in.

FIGURE 13. VARIATION IN CRACK-TIP MORPHOLOGY WITH DISTANCE FROM SURFACE OF SPECIMEN (d)

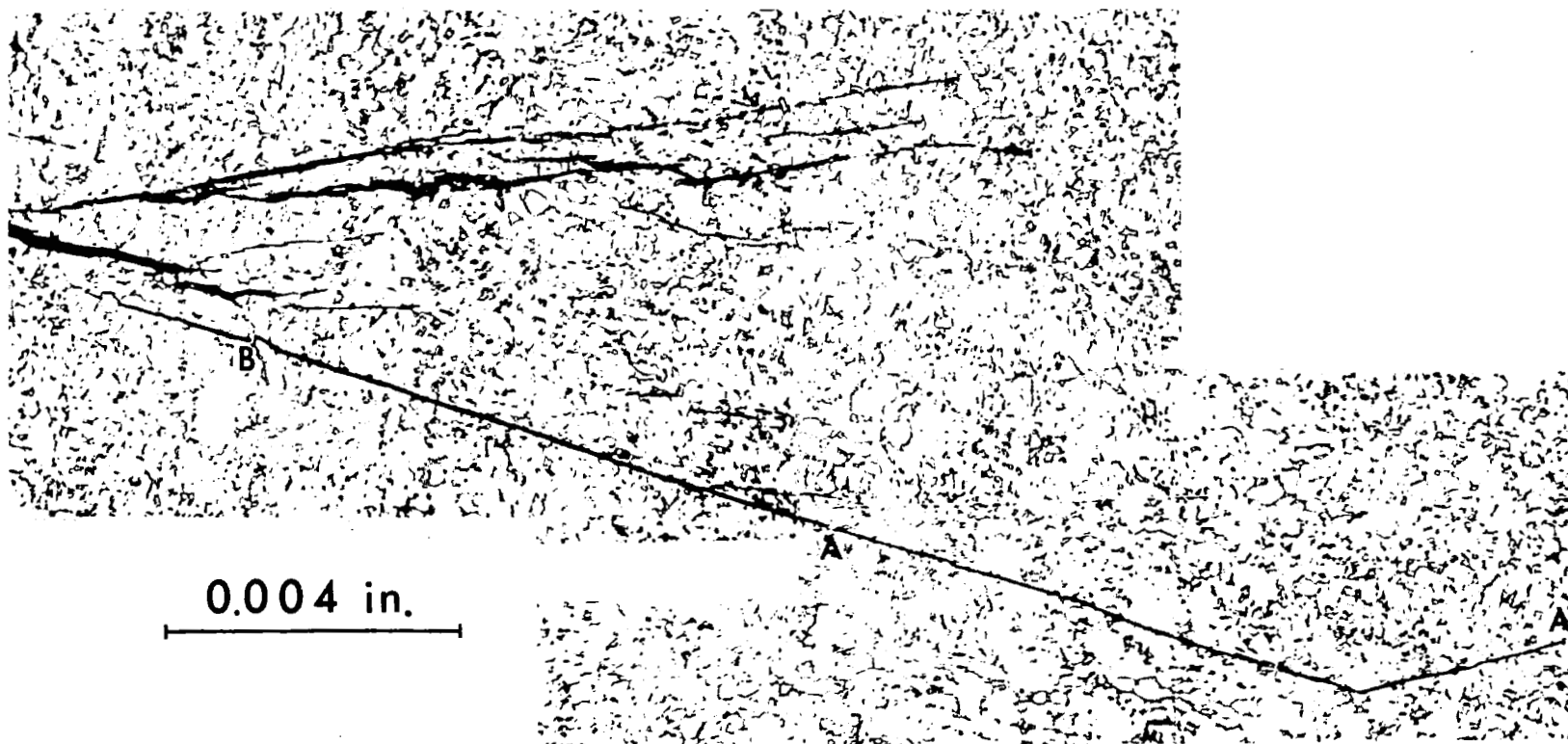
$$K_I = 53 \text{ ksi } \sqrt{\text{in.}}$$



a. "Ragged" Crack Morphology

FIGURE 14. DETAILS OF TWO DIFFERENT CRACK-TIP MORPHOLOGIES

$$K_I = 53 \text{ ksi} \sqrt{\text{in.}}$$



b. Severe Crack Branching

FIGURE 14. (Continued)

Ti-8 Al-1Mo -IV

3.5 % NaCl
 $K_I = 53 \text{ ksi } \sqrt{\text{in.}}$

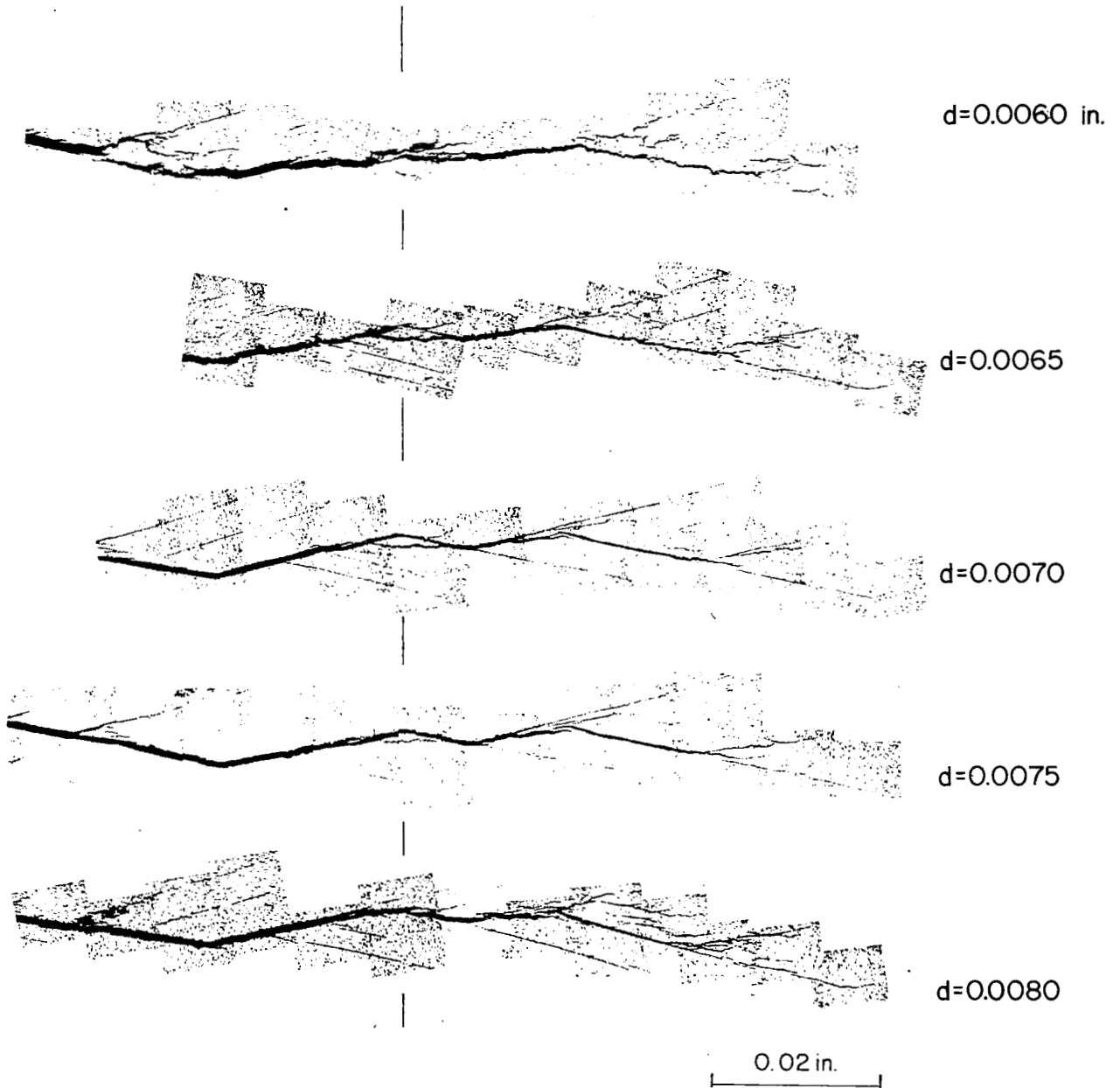


FIGURE 15. A THROUGH-THICKNESS SERIES OF MICROGRAPHS SHOWING THE WIDTH OF SEVERELY BRANCHED-CRACK SEGMENTS

Figures 13a, 13c, 13d and 14a, and accounted for the major proportion of the crack front.

- (2) Severely branched cracks that consisted of straight segments 0.020 to 0.040 inch in length. This type of morphology is illustrated in Figures 13b, 13e, and 14b. The individual branches were exceedingly straight; they rarely changed direction, and then only at beta particles (Figure 14b at A) or oddly shaped alpha grains (Figure 14b at B). They lay along directions which were inclined at approximately $\pm 30^\circ$ to the average crack propagation direction. The individual branches generally terminated at beta particles or grain boundaries. From the micrographs in Figure 15 the widths of the individual branches were estimated to be approximately 0.002 inch. Thus, the individual branches were long, narrow cracks approximately 1 grain diameter in width, having an aspect ratio of 10 to 20. The serial sectioning procedure revealed that the width of the areas of severely branched cracks was approximately equal to the width of the individual branches. The two crack morphologies alternated through the thickness of the specimen, the widths of the areas of "ragged" cracks being approximately twice that of the severely branched cracks.

Examinations of cracks of various lengths, (i. e., corresponding to various values of K_I at the crack tip) showed that areas of severe branching occurred only near the tips of cracks that had been subjected to high stress intensities. This could be seen by examining the whole length of a single crack. Severe branching was found only near the tip where the stress intensity had been highest. There was no evidence of severe branching toward the other end of the crack which had sustained only low stress intensities.

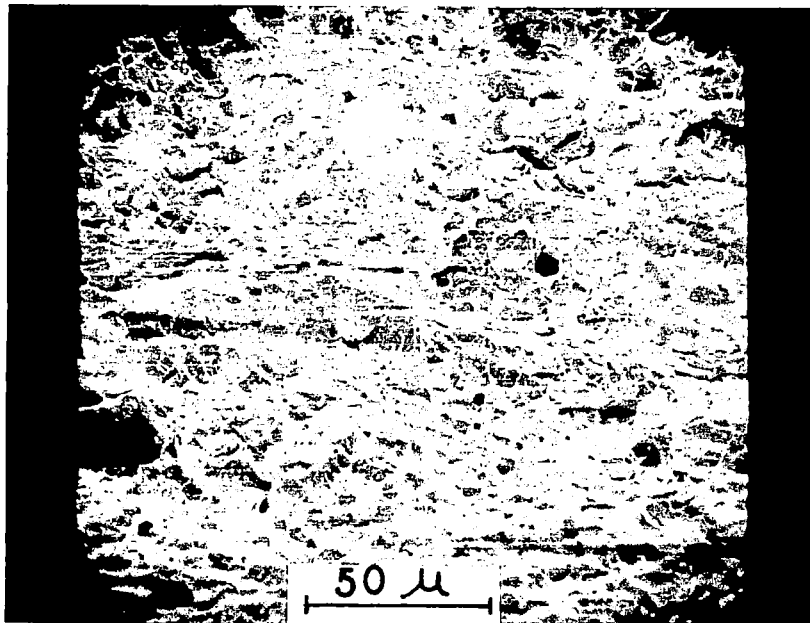


FIGURE 16. SCANNING ELECTRON MICROGRAPH OF AN AREA OF RAPID FRACTURE

Fractography. Scanning electron microscopy examination of fractured surfaces revealed certain features that were peculiar to the subcritical-cracking mechanism. Areas of rapid fracture exhibited the "cup-cone" failure mode* characteristic of ductile rupture (Figure 16). This was the case for rapid fracture in air as well as in aqueous environments. By contrast, the fracture surfaces resulting from subcritical cracking exhibited a high density of cleavage facets. In areas which had been subjected to a high stress intensity, ($> 2 K_{I_{SCC}}$), two distinct morphologies were observed. The first consisted of large, flat cleavage facets that tended to be elongated in the direction of crack propagation. This morphology is illustrated by the area at the top of Figure 17a (Area A), where the "river lines" running near to the average crack propagation direction are clearly visible. These facets were typically 50 to 200 microns long and 20 to 50 microns wide. Stereo microscopy revealed that these cleavage facets were not parallel to the macroscopic fracture surface. For example, the facet marked A (Figure 17a), is inclined such that it is down to the left and up to the right. The second morphology is illustrated by the area towards the bottom of Figure 17a (Area B). This fracture mode gave a much more irregular surface. There was still much evidence of cleavage, but here the cleavage facets were smaller (\approx the mean grain size), equiaxed, and inclined at various angles to the macroscopic fracture surface. There was also evidence of intergranular fracture, and deep crevices and pits. Another area illustrating this fracture mode is shown in Figure 17b.

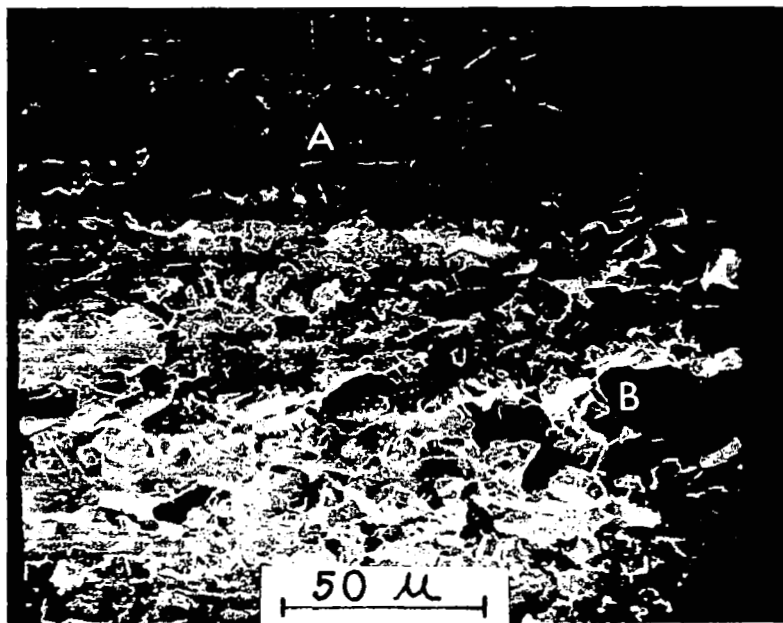
It is suggested that these two fracture modes correspond to the two types of crack-tip morphology which were observed by optical microscopy. That is, the areas containing the large cleavage facets correspond to areas of severe crack branching (the dimensions and orientation of the large cleavage facets are consistent with those of the individual branches), and the areas containing the smaller cleavage facets, pits, etc., correspond to the areas of "ragged" cracks. The ratio of the latter fracture mode to the former, as observed in the fractographs, was approximately 2:1, which is the same as the observed ratio of "ragged" cracks to severely branched cracks.

Studies of Crack-Tip Plastic Zones. The distribution of slip within the crack-tip plastic zone was clearly resolved by electron microscopy of the two-stage replicas. Figure 18 shows the slip-line pattern adjacent to a crack segment. (In a positive print of a two-stage replica, a crack intersecting the surface appears as a black line with a white shadow on one side. In Figure 18 the crack runs along the direction A-A.) The size of the plastic zone, ρ , was estimated by measuring the distance ahead of the crack tip beyond which slip lines were not observed. There was no systematic variation in ρ with applied stress intensity. The measured value of ρ was approximately 250 microns for the whole range of stress intensities investigated ($K_I = 20$ to $45 \text{ ksi}\sqrt{\text{in.}}$). The slip was invariably nonhomogeneous. That is, it occurred as coarse straight slip bands. Figure 19 shows this type of slip in detail. Occasionally, in the vicinity of a crack the slip bands were wavy (e.g., Figure 18 at X). The variations in slip-step height and slip-band spacing with K_I were measured, and the results are given in Table 9. The slip-step heights were measured from slip lines which appear white in positive prints, using the formula,

$$h = w \tan \phi / \sin \theta, \quad (4)$$

where h is the slip-step height, w is the measured width of the slip line, ϕ is the angle of incidence of the shadowing material on the specimen surface, and θ is the angle between the slip line and the projection of the shadowing direction on the specimen surface (see Figure 20).

*Note that areas which appear as "cup-cone" failures in scanning electron micrographs would appear as "dimpled" failures in electron micrographs of surface replicas.



a.



b.

FIGURE 17. SCANNING ELECTRON MICROGRAPHS FROM AREAS OF STRESS-CORROSION FRACTURE

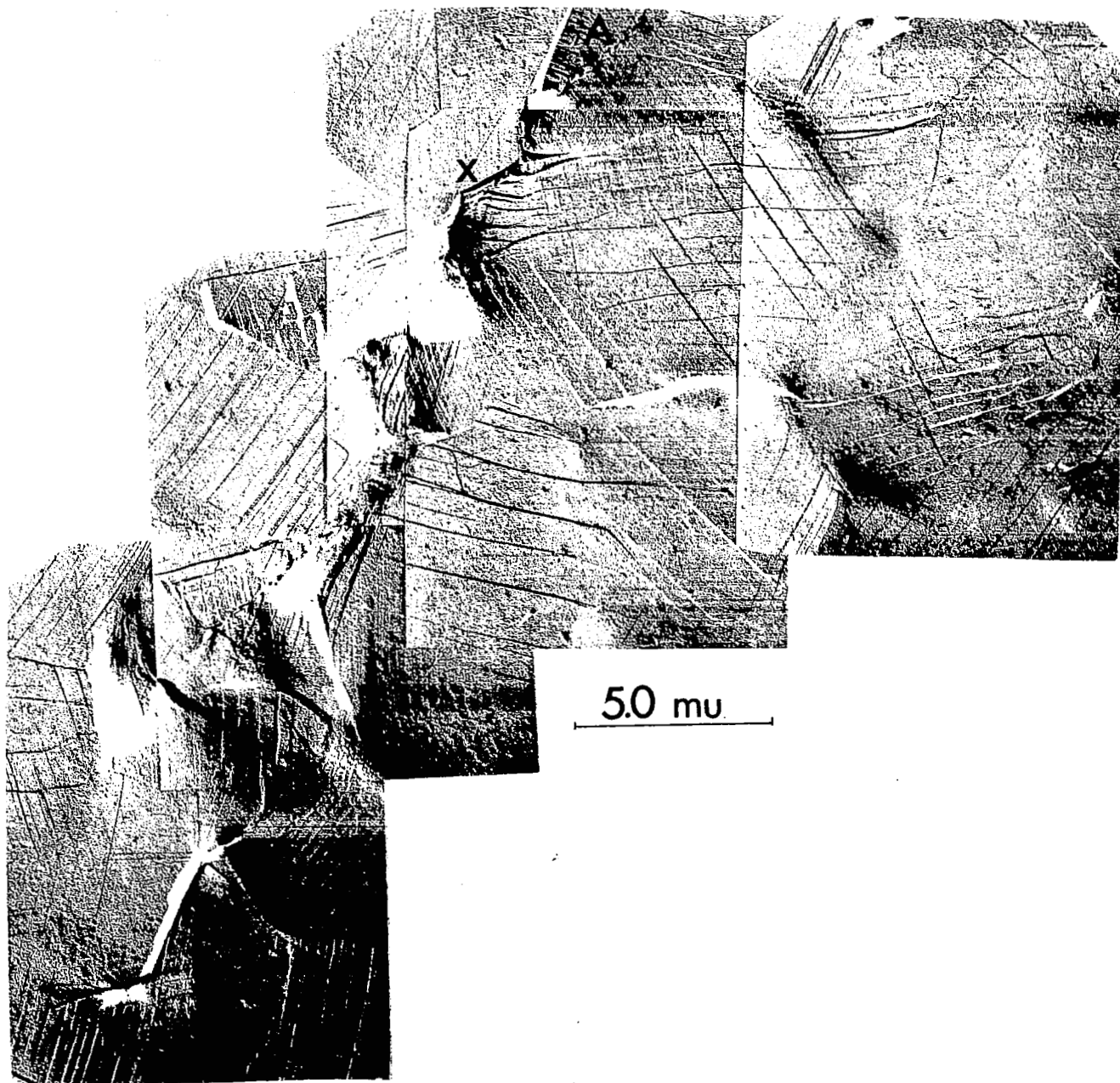


FIGURE 18. ELECTRON MICROGRAPH OF A TWO-STAGE CARBON REPLICA, ILLUSTRATING THE DISTRIBUTION OF SLIP AROUND A STRESS-CORROSION CRACK

$$K_I = 45 \text{ ksi } \sqrt{\text{in.}}$$

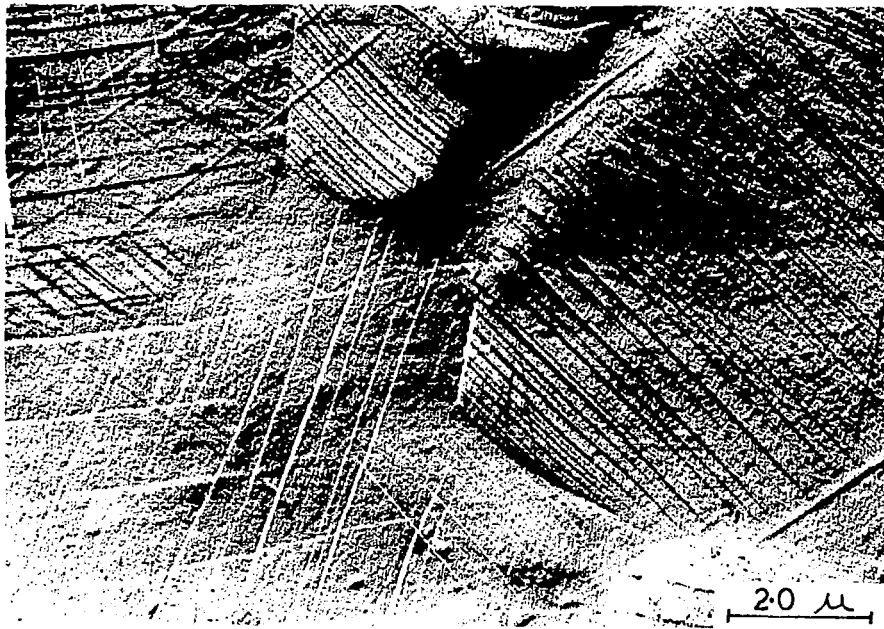


FIGURE 19. NONHOMOGENEOUS SLIP IN THE PLASTIC ZONE OF A STRESS-CORROSION CRACK

$$K_I = 53 \text{ ksi}\sqrt{\text{in.}}$$

Discussion

General Observations. The following general observations can be made on the phenomenology of stress-corrosion cracking of titanium alloys in aqueous environments:

- (1) There is a threshold stress intensity, $K_{I_{SCC}}$, below which subcritical crack growth does not take place. $K_{I_{SCC}}$ is sensitive to the chemistry of the environment, but it is independent of the temperature of the environment (over the limited range of temperatures which can be investigated). Other work not reported here has shown that $K_{I_{SCC}}$ is also dependent on alloy composition^(1, 2), heat treatment⁽²⁾, and applied electrode potential⁽⁷⁾. A finite plane-strain region at the crack front is required for subcritical cracking to proceed⁽¹¹⁾; hence, in thin sections, $K_{I_{SCC}}$ increases rapidly with decreasing specimen thickness.
- (2) The subcritical crack velocities are very high (10^{-3} – 10^{-2} in./sec).
- (3) The subcritical crack velocity is initially dependent on the applied stress intensity (Stage I), but at higher stress intensities the crack velocity approaches a constant value which is independent of K (Stage II).

TABLE 9. MEASURED SLIP-STEP HEIGHTS AND SLIP-BAND SPACINGS

Grain	No. of Slip Bands Measured	Average Slip-Step Height, A	Average Slip-Band Spacing, A
<u>$K_I = 20 \text{ Ksi}\sqrt{\text{In.}}$</u>			
1	38	42	950
2	45	36	1330
3	13	340	4520
4	10	130	5000
5	21	50	1080
		Mean $120 \pm 115 \text{ A}$	Mean $2580 \pm 1800 \text{ A}$
<u>$K_I = 35 \text{ Ksi}\sqrt{\text{In.}}$</u>			
1	54	127	1890
2	19	245	3940
3	24	84	1560
4	22	94	1270
5	13	70	3470
6	50	158	2430
7	10	258	5000
8	29	258	3720
9	29	76	1900
10	19	71	2590
		Mean $144 \pm 76 \text{ A}$	Mean $2780 \pm 1150 \text{ A}$
<u>$K_I = 45 \text{ Ksi}\sqrt{\text{In.}}$</u>			
1	33	64	1350
2	6	49	6170
3	9	72	5210
4	11	53	2580
5	43	77	1090
6	21	53	1420
7	26	59	1500
		Mean $61 \pm 10 \text{ A}$	Mean $2760 \pm 1920 \text{ A}$
<u>$K_I = 53 \text{ Ksi}\sqrt{\text{In.}}$</u>			
1	57	142	1340
2	11	113	4830
3	28	152	1420
4	7	129	3330
5	64	94	1260
		Mean $126 \pm 21 \text{ A}$	Mean $2440 \pm 1420 \text{ A}$

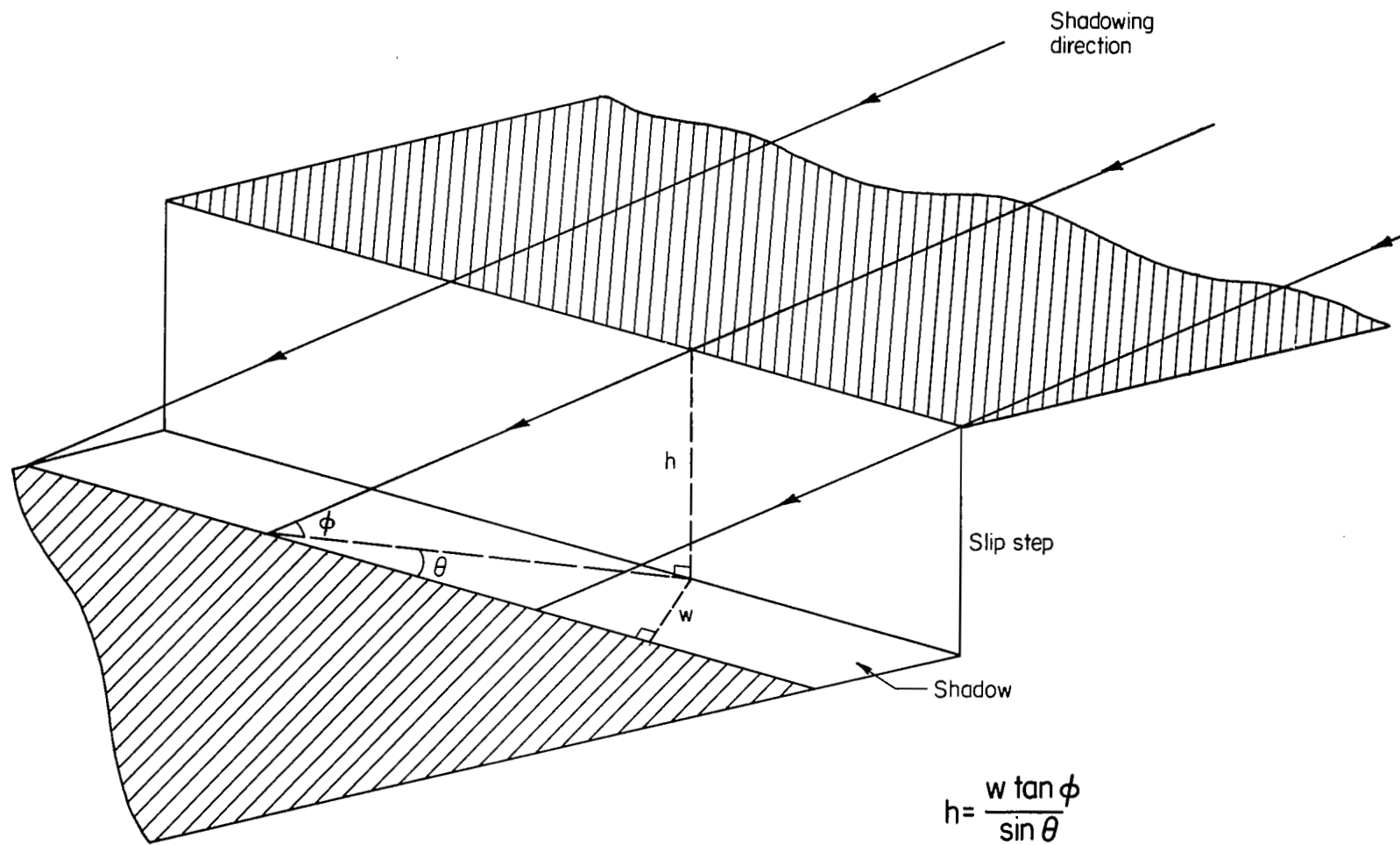


FIGURE 20. CALCULATION OF SLIP-STEP HEIGHT, h , FROM SLIP-LINE WIDTH, w

- (4) During subcritical cracking the cracks follow a predominantly transgranular path. At high stress intensities the main crack front is branched, and consists of numerous long (~ 0.030 inch), narrow (~ 0.002 inch), exceedingly straight transgranular cracks.
- (5) The fracture surfaces resulting from subcritical crack growth contain a high density of cleavage facets. By contrast, areas of rapid fracture have the "dimpled" appearance characteristic of ductile rupture.

All mechanisms of environment-assisted crack growth can be placed in one of two categories:

- (1) Crack extension is the direct result of an electrochemical reaction
- (2) Crack extension occurs by a conventional metallurgical fracture mechanism.

The difficulty in identifying the precise mechanism of crack extension in a stress-corrosion situation is that, by definition, both electrochemical and metallurgical factors are involved. The problem is to identify the step in this complex interaction that is responsible for crack extension. Generally this is prohibitively difficult, but in certain cases the mechanism of crack extension can be identified. A useful parameter in this respect is the magnitude of the subcritical crack velocity. Table 10 lists typical magnitudes of subcritical crack velocities for a variety of materials and environments. The list spans six orders of magnitude, and the crack-extension mechanism can be defined with reasonable certainty for the two extremes of crack velocity. At the low-crack-velocity end of the list, crack extension is usually the direct result of an electrochemical reaction. Examples of this behavior are the localized anodic dissolution along slip bands in the case of stainless steels in chloride environments⁽⁶⁾, and the repeated formation and rupture of an anodic film in the case of alpha brass in aqueous ammonia.⁽⁷⁾ At the high-velocity end the rates of crack extension are too high to be the direct result of an electrochemical reaction. In this regime the environment interacts with the metal to produce a conventional metallurgical fracture at a low stress. A good example of this behavior is the embrittlement of aluminum by liquid mercury, where the environment adsorbs on the base metal at the crack tip and lowers the local cleavage strength.⁽¹⁰⁾ (Strictly speaking, this is not stress-corrosion cracking since there is no electrochemical reaction between the metal and the environment.)

At intermediate values of crack velocity the distinction between metallurgical failure mechanisms and electrochemical mechanisms is not so obvious. However, for alpha-rich, alpha + beta titanium alloys, such as Ti-8Al-1Mo-1V, in aqueous environments, the evidence suggests strongly that the mechanism of crack extension is environment-induced cleavage of the alpha grains. Direct observation of stress-corrosion cracks and fracture surfaces reveal a preponderance of transgranular cleavage facets in the alpha grains, in contrast with the "dimpled" ductile rupture which results from supercritical cracking. In addition, the typical subcritical-crack velocities are too high to be achieved directly by an electrochemical reaction alone. A simple calculation reveals that a corrosion current density of 100 amp/cm^{-2} would be required to achieve a crack velocity of 10^{-3} in./sec by anodic dissolution.

TABLE 10. TYPICAL VALUES OF FRACTURE TOUGHNESS AND SUBCRITICAL-
CRACK VELOCITY FOR SELECTED MATERIALS AND ENVIRONMENTS

Material	Fracture Toughness, ksi $\sqrt{\text{in.}}$		Subcritical-Crack Velocity, in./sec
	Air	Environment	
18-8 stainless steel		42% MgCl ₂ at 150 C	10 ⁻⁶
Cu-30 Zn		15 N aqueous ammonia	10 ⁻⁵
7075 aluminum alloy	K _c = 20	K _{scc} = 6 (3.5% NaCl)	10 ⁻⁵
Glass	K _c = 0.7	K _{scc} = 0.4 (moist air, 100% R.H.)	10 ⁻⁵
AgCl		17 N AgNO ₃ + AgCl ²⁺	10 ⁻⁵
D6aC steel, hydrogenated	K _c = 70	K _I = 40 (air)	10 ⁻⁵
H-11 steel	K _c = 45	K _{scc} = 20 (moist air, 100% R.H.)	10 ⁻⁴
H-11 steel	K _c = 45	K _{scc} = 10 (dry hydrogen gas)	10 ⁻⁴
Ti-8Al-1Mo-1V	K _c = 60	K _{scc} = 20 (3.5% NaCl)	10 ⁻³
2024 aluminum alloy		Liquid Hg	1

This is not to say that the electrochemical reaction is not necessary and important. The dependence of subcritical-crack velocity on applied electrode potential⁽⁵⁾, and the high acidity of the aqueous environment near the crack tip⁽¹¹⁾ establish that an electrochemical reaction is both necessary and important to the kinetics of cracking. However, it is suggested that the electrochemical reaction plays an indirect, rather than a direct, role in the crack-extension mechanism. Specifically, it is suggested that the electrochemical reaction between titanium and the aqueous chloride solution produces an embrittling species (which is at present not identified). The embrittling species then migrates from its point of origin to the crack-tip region of the metal, and cleavage occurs in the alpha grains subjected to the maximum tensile test. Thus, the process may be divided into three steps, any of which could be rate-controlling:

- (1) Production of the embrittling species by the electrochemical reaction
- (2) Transportation of the embrittling species to the crack tip
- (3) Cleavage of the alpha grains at the point of maximum tensile stress.

Unfortunately, few details are positively known for any of these steps. The embrittling species is not known, nor are the pertinent chemical reactions or the precise electrochemical conditions under which these reactions occur. It is not known

where the embrittling species is produced or its path to the crack tip, i. e., whether it migrates through the electrolyte, along the crack surface, or through the bulk of the metal. The necessity for plane-strain loading indicates that the cleavage cracks nucleate in the plain-strain region ahead of the crack tip where the tensile stress is highest.⁽¹²⁾ This would suggest that the embrittling species dissolves in the metal and diffuses ahead of the instantaneous location of the crack tip, ruling out the possibility of adsorption. In support of this model, Katz and Gerberich⁽¹³⁾ have recently reported that discontinuous crack propagation in titanium alloys has been detected by acoustic-emission measurements. In the present work no evidence was found of isolated cracks ahead of the main crack front. All of the apparently isolated cracks in Figures 13 through 15, upon serial sectioning, were found to connect with branches of the main crack. However, this result is not definitive because, if the distance between the crack front and the region of maximum tensile stress is of the order of the average grain diameter, then it is unlikely that any isolated cracks could be found. This indecisive evidence coupled with the fact that the stress distribution at the crack tip over distances of the order of the grain size is not known means that at present no conclusions can be drawn concerning the exact crack-initiation site. Finally, the precise rate of the embrittling species in causing cleavage is not known. Here there are two possibilities:

- (1) The embrittling species lowers the cleavage strength of alpha-titanium either by dissolving in the metal and diffusing to the plane-strain plastic zone, or by adsorbing on the base metal near the crack tip.
- (2) The embrittling species somehow raises the stress required to create and move dislocations in the plane-strain plastic zone, and hence raises the maximum tensile stress above the intrinsic cleavage strength of the material.

Analysis of Crack-Velocity Data. Despite all of these uncertainties, the qualitative model described above can be used to predict the relationship between subcritical-crack velocity and applied stress intensity. Consider first the case where the embrittling species dissolves in the metal and lowers its cleavage strength. Assuming an inverse proportionality between the local cleavage strength in the plane-strain plastic zone, σ^* , and the local concentration of embrittling species, X^* , gives:

$$\sigma^* = \sigma_f^* - \left(\frac{\sigma_f^* - \sigma_i^*}{X_i^*} \right) \cdot X^*, \quad (5)$$

where σ_f^* is the intrinsic cleavage strength of the metal ($X^* = 0$), and σ_i^* is the minimum cleavage strength of the metal - x system which obtains for $X^* \geq X_i^*$ (solid line in Figure 21). The maximum tensile stress in the plane-strain plastic zone, σ , can be related to the applied stress intensity, K_I , as follows⁽¹⁴⁾:

$$\sigma = Y + \alpha K_I, \quad (6)$$

where Y is the tensile yield stress and α is a constant approximately equal to 2. Thus, Equation (5) can be written:

$$X^* = \frac{K_{I_f}^* - K_I^*}{K_{I_f}^* - K_{I_i}^*} \cdot X_i^*. \quad (7)$$

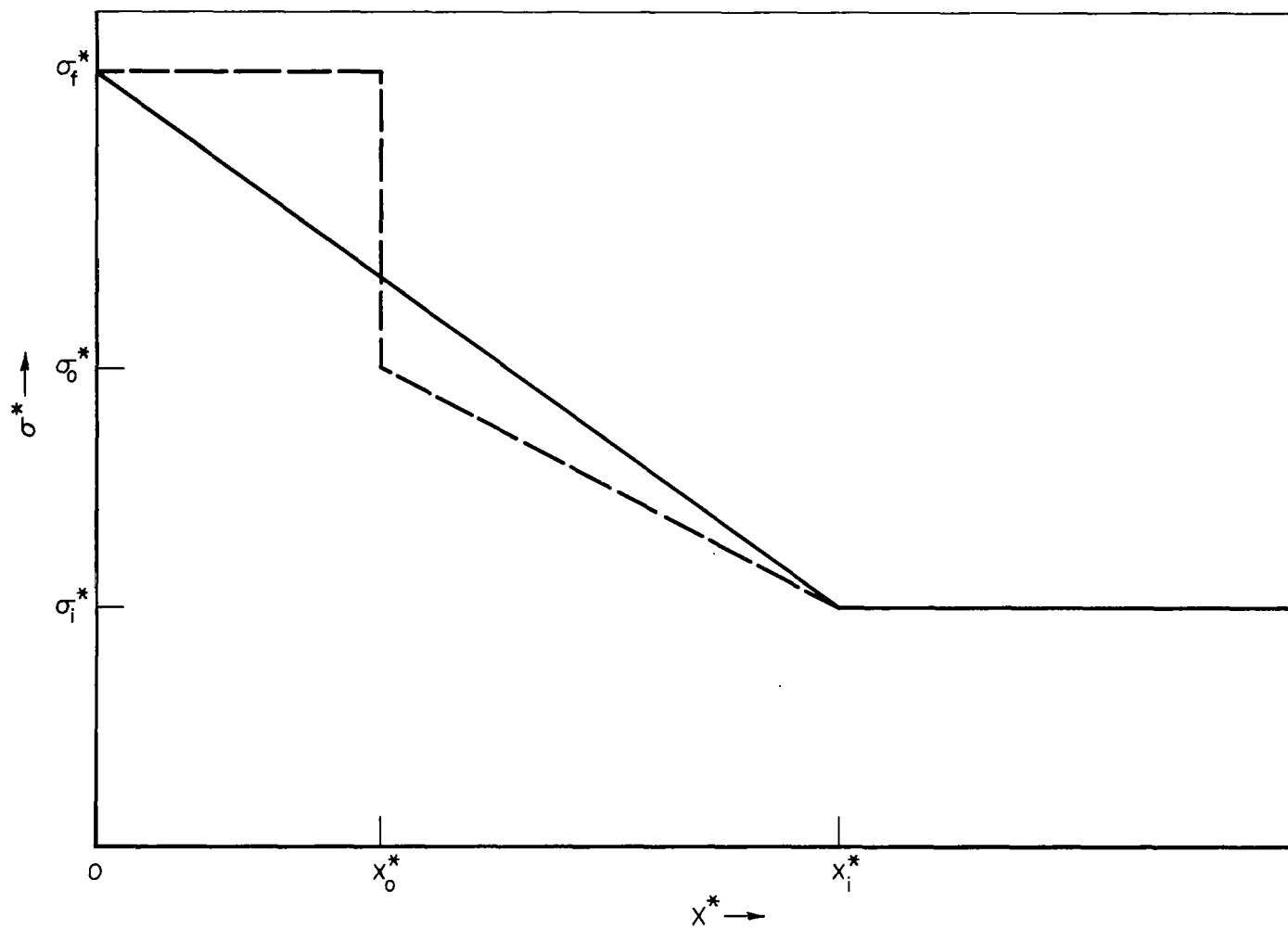


FIGURE 21. IDEALIZED VARIATION IN CLEAVAGE STRENGTH WITH CONCENTRATION OF EMBRITTLING SPECIES

Exactly the same expression is obtained if σ^* is constant and Y is linearly proportional to X^* . In other words, from the crack-velocity data alone it is not possible to determine whether the embrittling species lowers the cleavage strength or increases the yield stress of alpha titanium.

When $K_I < K_{I_i}^*$, no crack extension occurs, ($K_{I_i}^* \equiv K_{I_{scc}}$). When $K_I > K_{I_f}^*$, supercritical cracking occurs ($K_{I_f}^* \equiv K_{I_x}$). When $K_{I_{scc}} \leq K < K_{I_x}$, subcritical cracking occurs. The observed variation in $K_{I_{scc}}$ with yield stress is consistent with this qualitative model. Equation (6) predicts that for a given cleavage strength, σ^* , $K_{I_{scc}}$ should vary inversely with yield stress as follows:

$$K_{I_{scc}} = \frac{1}{\alpha}(\sigma^* - Y). \quad (8)$$

Figure 22 shows such a plot for a series of Ti-Al base alloys in which the yield stress was varied by different amounts and combinations of beta-stabilizing alloy additions.⁽¹⁾ It is assumed that the cleavage strength of the alpha phase does not vary significantly over this narrow range of composition. The best-fit straight line for these data (least-squares method) gives a relationship:

$$K_I = \frac{1}{2.3} (180 - Y). \quad (9)$$

The term α is ≈ 2 as it should be, and the calculated cleavage stress is 180 ksi.

During subcritical cracking, the local concentration of the embrittling species required for crack extension is given by Equation (7) when $K_I^* = K_I$, i. e.,

$$X^* = \frac{K_{I_x} - K_I}{K_{I_x} - K_{I_{scc}}} \cdot X_i^*. \quad (10)$$

This critical concentration is achieved by a flux of x from the environment into the plane-strain plastic zone. Consider the idealized crack tip shown in Figure 23, where C is the crack opening displacement and ρ is the length of the plane-strain plastic zone. If the flux of x through the surface A-A into the volume ρC (unit width) is J moles/(cm²)(sec), the rate of change of concentration of x in the plastic zone is

$$\frac{\Delta X}{\Delta t} = \frac{JC}{C\rho} = \frac{J}{\rho}, \quad (11)$$

and the time required to achieve the critical concentration, X^* , is given by

$$\int_0^{X^*} dx = \int_0^{t^*} \frac{J dt}{\rho}. \quad (12)$$

The maximum average crack velocity corresponds to the crack extending a distance ρ in time t^* , hence:

$$\begin{aligned} \dot{a} &= J/X^* \\ &= \frac{K_{I_x} - K_{I_{scc}}}{K_{I_x} - K_I} \cdot \frac{J}{X_i^*}, \end{aligned}$$

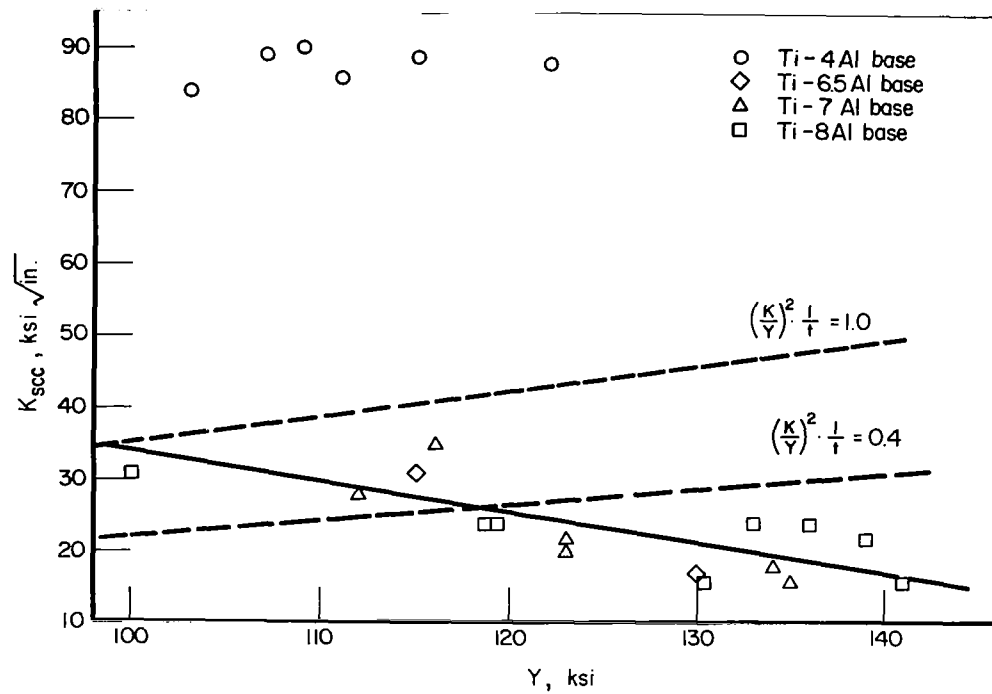


FIGURE 22. VARIATION IN $K_{I_{scc}}$ WITH YIELD STRESS FOR Ti-Al BASE ALLOYS

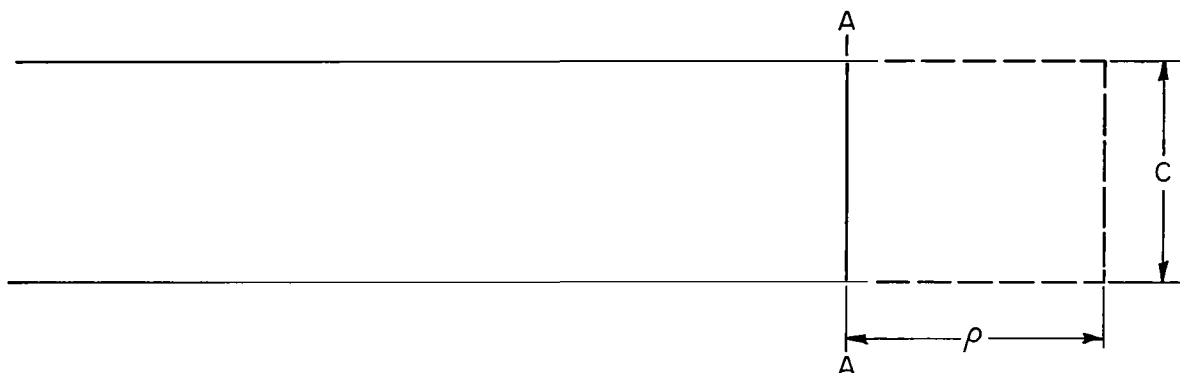


FIGURE 23. IDEALIZED CRACK TIP

which can be written

$$\begin{aligned}\dot{a} &= \frac{J}{X_1^*} \left(1 - \frac{K_{I_{sc}}}{K_{I_x}} \right) \left(\frac{1}{1 - K_I/K_{I_x}} \right) \\ &\approx \frac{J}{X_1^*} \left(\frac{1}{1 - K_I/K_{I_x}} \right).\end{aligned}\quad (13)$$

Equation (13) predicts that \dot{a} will increase exponentially with increasing K_I . However, for low values of K_I corresponding to Stage I of subcritical cracking, $K_I/K_{I_x} \ll 1$ and a linear approximation can be made:

$$\dot{a} \approx \frac{J}{X_1^*} \left(1 + \frac{K_I}{K_{I_x}} \right) \quad (14)$$

Equation (14) can be used to analyze the initial linear portions of the $\dot{a} - K_I$ curves (Stage I). The stress-independent parameter which was used was the initial slope of the $\dot{a} - K_I$ curves, $S_0 = (\partial \dot{a} / \partial K)_{K_I = K_{I_{sc}}} = K_{I_{sc}}$. The temperature dependence of S_0 is tabulated in Table 11 and plotted as $\log S_0$ against $1/T$ in Figure 24, whence the relationship

$$S_0 = 6.8 \exp(-5600/RT). \quad (15)$$

Similarly, the dependence of S_0 on the chloride-ion concentration is tabulated in Table 11. A plot of $\log S_0$ against $\log [Cl^-]$ yields a straight line (Figure 25), and suggests the relationship

$$S_0 = 7.1 \times 10^{-5} [Cl^-]^{0.17}. \quad (16)$$

Clearly, Equation (14) does not adequately describe Stage II of subcritical cracking. Several possible explanations for the stress-independent crack velocity are discussed below.

TABLE 11. SUMMARY OF DATA ON CRACK VELOCITIES FOR Ti-Al-1Mo-1V

T, K	[Cl ⁻], ppmw	K _{I_{SCC}} , ksi $\sqrt{\text{in.}}$	K _{I_B} , ksi $\sqrt{\text{in.}}$	K _{I_B} - K _{I_{SCC}} , ksi $\sqrt{\text{in.}}$	K _{I_X} , ksi $\sqrt{\text{in.}}$	$\frac{S_{O_2}}{5/2}$ /kip/sec 10 ⁻³ in.	\dot{a}^0 , 10 ⁻³ in./sec
272	2.1 x 10 ⁴	17.7	33.5	15.8	65.4	0.20	3.3
295	2.1 x 10 ⁴	14.0	27.5	13.5	67.4	0.44	6.2
333	2.1 x 10 ⁴	14.7	21.5	6.8	62.1	1.3	9.5
366	2.1 x 10 ⁴	18.4	21.0	2.6	66.3	3.0	15.9
295	1.0 x 10 ⁻¹	24.2	40.5	16.3	59.5	0.054	0.90
295	1.0 x 10 ²	20.8	39.0	18.2	58.7	0.12	2.4
295	6.0 x 10 ³	18.4	33.5	15.1	60.3	0.31	4.8
295	2.1 x 10 ⁴	14.0	27.5	13.5	67.4	0.44	6.2

First, it is possible that a certain minimum concentration of the embrittling species, X_O^* , is required before the cleavage strength is affected, and for concentrations in excess of this, σ^* decreases linearly with X^* up to the limiting value X_i^* . This behavior is illustrated by the broken line in Figure 21. Thus, when the maximum tensile stress, σ , is greater than σ_O^* , the critical concentration remains constant at X_O^* , and the limiting crack velocity, \dot{a}^0 , is given by

$$\dot{a}^0 = J/X_O^*. \quad (17)$$

The variation in \dot{a}^0 with the environmental variables T, and [Cl⁻] can also be determined from the data in Table 11. (Where necessary, \dot{a}^0 was estimated by extrapolating the experimental \dot{a} - K_{I_X} curve past K_{I_X} .) Log \dot{a}^0 is plotted against 1/T in Figure 26, whence the relationship

$$\dot{a}^0 = 1.2 \exp (-3200/RT). \quad (18)$$

Log \dot{a}^0 is plotted against log [Cl⁻] in Figure 27, which gives the relationship

$$\dot{a}^0 = 1.2 \times 10^{-3} [\text{Cl}^-]^{0.16}. \quad (19)$$

Comparison of Equations (15) and (18) and Equations (16) and (19) suggests that the temperature dependence is different in Stage I cracking from that in Stage II, but the dependence on chloride-ion concentration is the same in both cases. From Equations (14) and (17) it is to be expected that in both cases the observed temperature and chemistry dependences arise solely from the flux term J. The terms X_i^* , X_O^* , and K_{I_X} are essentially material constants which should not vary much with the chemistry of the environment or with temperature over the limited range of temperatures investigated. Thus, the flux of the embrittling species to the crack tip is determined by at least two distinct processes, and the rate-limiting process changes upon going from Stage I to Stage II. Wiederhorn⁽¹⁴⁾ has reported similar behavior for subcritical cracking in ceramic materials. He ascribed the environmental dependence of \dot{a} in Stage I to an activated process at the crack tip, and the dependence in Stage II to a transport rate-limited process. Applying this reasoning to the present case, the rate-limiting process in Stage I cracking would be a reaction at the crack tip, such as dissolution of the embrittling species in the metal, adsorption, or diffusion in the plastic zone, and the rate-limiting process in Stage II would be diffusion of the

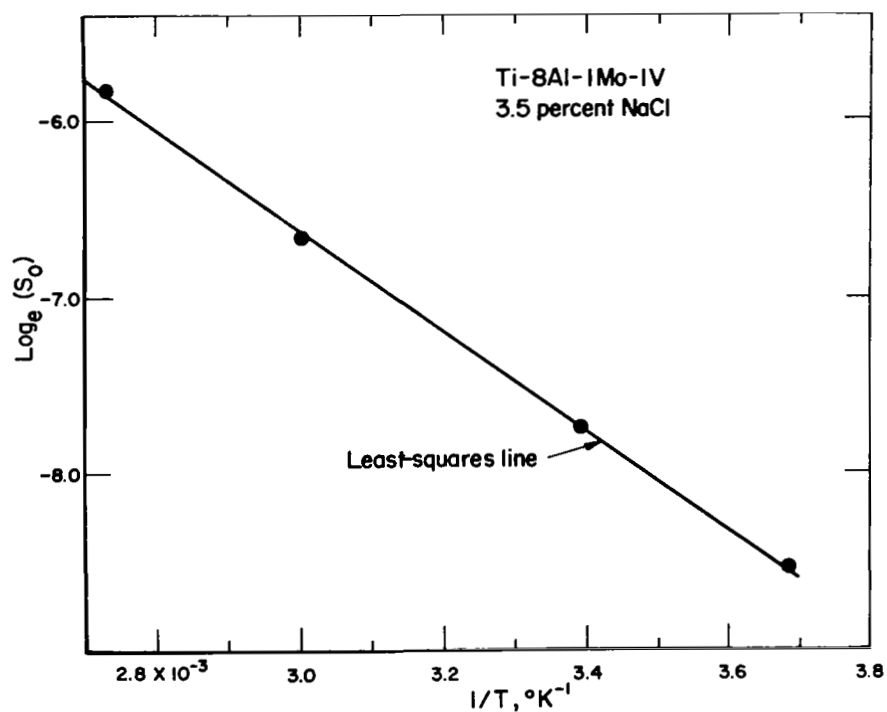


FIGURE 24. TEMPERATURE DEPENDENCE OF S_0

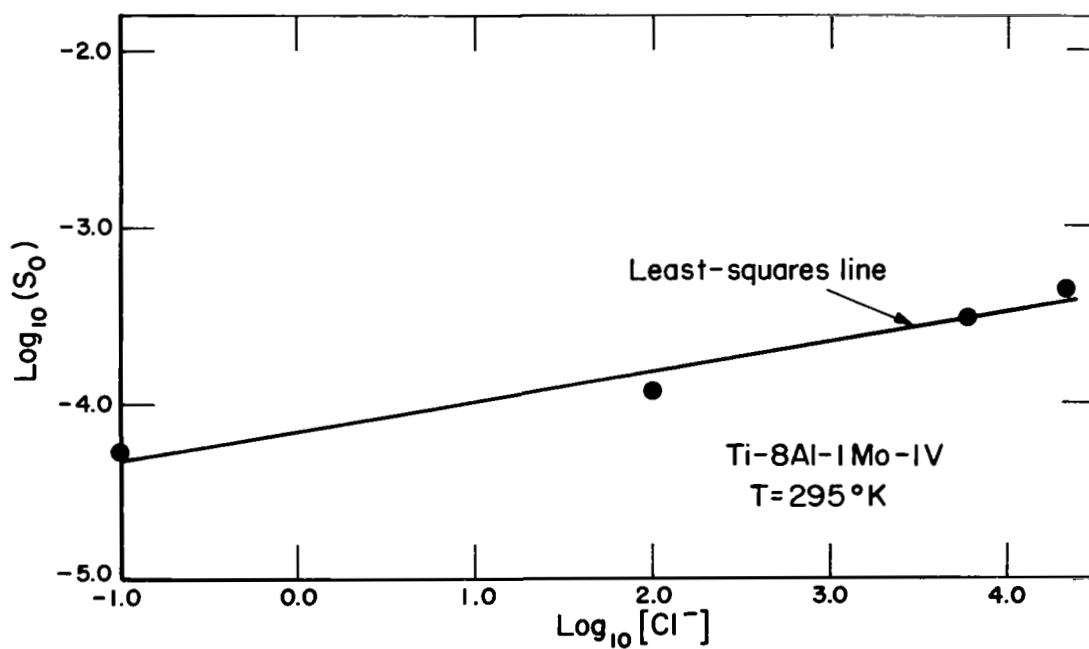


FIGURE 25. VARIATION IN S_0 WITH CHLORIDE-ION CONCENTRATION

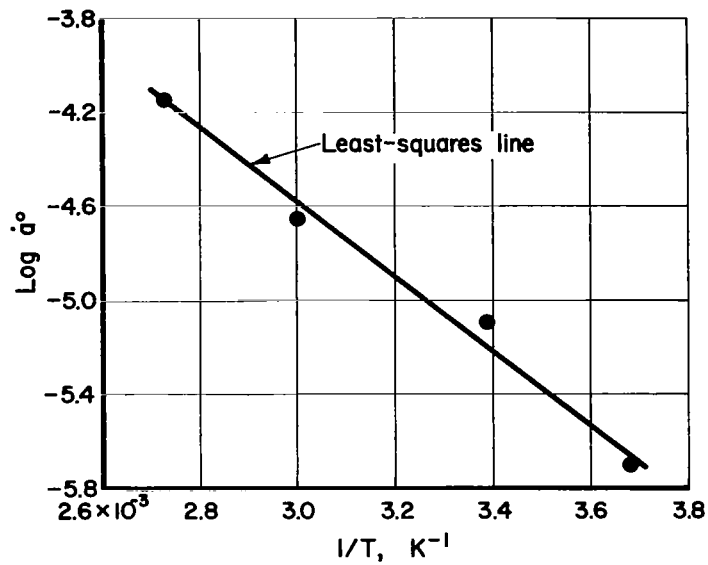


FIGURE 26. TEMPERATURE DEPENDENCE OF a°

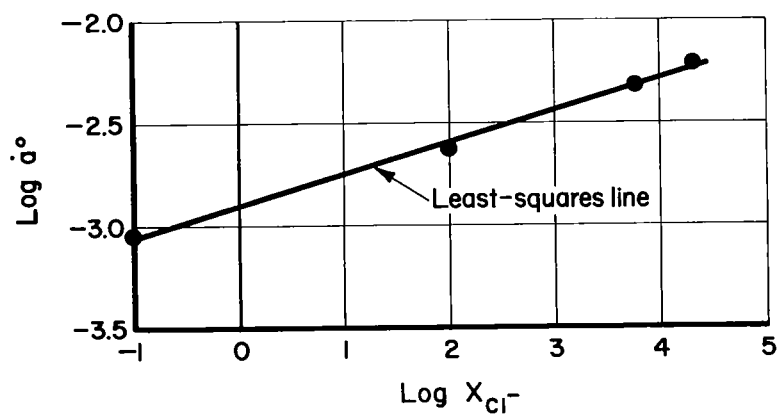


FIGURE 27. VARIATION IN a° WITH CHLORIDE-ION CONCENTRATION

embrittling species from its point of origin to the crack tip. Thus, the activation energy of the transport reaction is 3200 cal/gm-mole, and the activation energy of the crack-tip reaction is 5600 cal/gm-mole.

This interpretation of Stages I and II of subcritical cracking must remain tentative because it is not certain that the environmental dependences of S_0 and \dot{a}^0 are entirely due to the flux term. If K_{IB} is taken to be the applied stress intensity when $\dot{a} = \dot{a}^0$, then from Equations (14) and (17),

$$K_{IB} - K_{Isc} = \frac{X_i^* K_{IC}}{X_o^*}. \quad (20)$$

K_{IB} was estimated for each set of conditions by extrapolating the initial linear portion of the $\dot{a} - K_I$ curve to the point where $\dot{a} = \dot{a}^0$, and the results are given in Table 11. From these data it can be seen that $(K_{IB} - K_{Isc})$ is essentially independent of $[Cl^-]$ as expected, but $(K_{IB} - K_{Isc})$ is definitely temperature dependent. This implies that the term $X_i^* K_{IC} / X_o^*$ varies with temperature, and, hence, the observed "activation energies" are influenced by factors other than the flux term. However, the principal objection to this interpretation is that it is contrived to agree qualitatively with the observations, and there is no direct evidence that the proposed model is accurate.

A second possibility is that Stage II of subcritical cracking is associated with the onset of crack branching. This has been found to be the case for subcritical cracking of high-strength steels⁽¹⁵⁾, aluminum alloys⁽¹⁶⁾, and titanium alloys⁽¹⁶⁾, when tested in aqueous chloride environments. A rigorous theory of crack branching during subcritical cracking is not presently available, but the following empirical conditions have been established^(15,16):

- (1) When crack branching occurs, the subcritical-crack velocity is independent of applied stress intensity.
- (2) For branching to occur, a critical applied stress intensity is necessary, which is generally 2 to 4 times the stress intensity required to initiate subcritical cracking.

In the present work, severely branched cracks were found only at high stress intensities in the range of Stage II. By inspecting the total length of arrested cracks it was verified that the onset of severe crack branching occurred at crack lengths corresponding to stress intensities in the region of transition from Stage I to Stage II. This metallographic evidence suggests strongly that Stage II cracking behavior results from the propagation of severely branched cracks. If this is the case, then K_{IB} refers to the critical stress intensity for the onset of severe crack branching, and \dot{a}^0 simply represents the value of \dot{a} when $K_I = K_{IB}$. Experimentally, K_{IB}/K_{Isc} varies from 1.1 to 2.0 (Table 11). In this case \dot{a}^0 is not a very useful parameter for analyzing the kinetics of subcritical cracking, since it depends on K_{IB} which cannot be evaluated quantitatively.

Another explanation of Stage II cracking, which leads to the same conclusions as the crack-branching explanation, is that the state of stress at the crack tip changes during crack propagation. It was shown earlier that the specimen thickness was sufficient for plane-strain conditions to persist at the crack tip up to final fracture. However, the formula used to calculate K_I [Equation (1)] is not valid for long cracks⁽¹⁷⁾. Thus, it is possible that the calculated stress intensities are not accurate in the region of Stage II cracking. If this is the case, then, as with the crack-branching hypothesis,

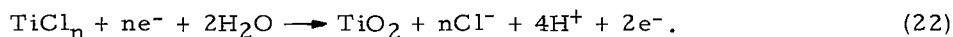
the onset of Stage II cracking is caused by a mechanical effect, and is not directly associated with the stress-corrosion-cracking mechanism.

In view of the direct evidence of severe crack branching provided by the metallographic studies, the second explanation of Stage II cracking is preferred. However, there is considerable uncertainty about this point, and subsequent discussion of the kinetics of subcritical cracking will be confined to Stage I.

The relationship between subcritical-crack velocity and applied stress intensity found in the present work is qualitatively the same as that found by other workers for titanium alloys in neutral salt solutions^{(4)*}. The apparent activation energy of 5600 cal/gm-mole for Stage I cracking is also in agreement with the findings of other workers⁽⁴⁾. The magnitude of this apparent activation energy is consistent with a surface reaction (diffusion or adsorption) and with the bulk diffusion of hydrogen in beta titanium, ($Q_H = 6600$ cal/gm-mole). The dependence of \dot{a} on the 1/6 power of the average chloride-ion concentration in the environment is similar to the finding of Beck⁽⁵⁾ who reported a $[Cl^-]^{1/4}$ dependence. The significance of the numbers 1/6 or 1/4 is not understood. However, the observed dependence of \dot{a} on $[Cl^-]$ supports Beck's hypothesis that the electrochemical reaction which takes place at the crack tip (anodic reaction) is between titanium and a halide ion:



The chloride (which has not been positively identified) is either water soluble or sufficiently permeable that the metal surface is not passivated before crack extension occurs. The chloride is eventually hydrolyzed, and a stable oxide forms on the crack sides:



Thus, there is a flux of chloride ions to the crack tip [as described by Beck⁽⁵⁾], and there is an increase in hydrogen-ion concentration in the electrolyte in the vicinity of the crack tip. The latter point is consistent with the observation of Brown et al.⁽¹¹⁾ that the electrolyte has a pH of approximately 2 near the tip of a propagating stress-corrosion crack. Note that the obvious embrittling species resulting from these reactions is hydrogen. The H^+ ions produced by the hydrolysis of the titanium chloride will migrate to cathodic sites on the crack sides and form atomic hydrogen by acquiring an electron:



Observations of Crack-Tip Morphologies. The transgranular cracks observed metallographically (Figures 13 through 15) and the flat facets seen in the fracture faces (Figure 17) have all the appearances of cleavage cracks. The cleavage fracture mode for subcritical cracking of titanium alloys in aqueous environments is well established^(8,18). The cleavage plane has been found independently by several investigators^(8,18) to be approximately the $\{10\bar{1}8\}_\alpha$ plane. The significance of this high index cleavage plane is not clear. Mauney and Starke⁽¹⁹⁾ have shown, using Stroh's theory, that the maximum tensile stress due to dislocation pileups in slip systems of the type

*Blackburn et al.⁽⁴⁾ have summarized available crack-velocity data in their recent review of titanium stress-corrosion cracking. However, note that a slightly different nomenclature is used in the present report. What is referred to as Stage I in this report corresponds to Stage II-A in Blackburn et al.'s description. Their Stage I refers to the extremely slow crack growth which occurs in highly acidic solutions, but not in neutral salt solutions.

$\{11\bar{2}2\} \langle 11\bar{2}3 \rangle$ is approximately perpendicular to $\{10\bar{1}8\}$. They suggest that this slip system is active during subcritical cracking because slip is impeded on $\{10\bar{1}0\} \langle 11\bar{2}0 \rangle$ and $\{10\bar{1}1\} \langle 11\bar{2}0 \rangle$ by hydride precipitation.

The "ragged" crack morphology which is characteristic of Stage I crack propagation (Figure 14a) is a result of the cleavage fracture mode. The cracks exhibiting this morphology propagate along branched segments approximately 0.004 – 0.008 inch in length. In an individual section perpendicular to the crack front, many of the individual segments appear to be isolated from each other. However, serial sectioning established that they are all interconnected. At the tip of each individual segment, the direction of the crack changes slightly from one grain to another owing to the misorientation between the grains, and, hence, between the preferred cleavage planes. Thus, the crack front is not a single line, but, rather, it consists of several interconnected segments of cracks which contain areas or "ligaments" of uncracked material. The ligaments must offer some resistance to crack opening, and probably account for the areas of ductile rupture seen in the fractographs.

By contrast, the severely branched cracks which are found during Stage II cracking consist of long (0.020 – 0.040 inch), narrow (~0.002 inch), transgranular segments which are extremely straight. These long fingers appear to lie along two preferred directions which make angles of approximately ± 30 degrees with the macroscopic crack propagation direction. The length of the "fingers" is quite remarkable, and has not been satisfactorily explained. It appears that each individual finger results from a single cleavage event, but it is difficult to explain how an environment-induced cleavage crack can run with little change in direction through approximately 50 grains. It would seem that for this to occur, two conditions are necessary:

- (1) The material has a strong preferred orientation such that the preferred cleavage planes are nearly parallel in all the alpha grains.
- (2) The embrittling species diffuses into the metal a distance of the order of 50 grain diameters. (This would also support the hypothesis that hydrogen is the embrittling species.)

The preferred orientation in the specimen material was not determined rigorously, but diffractometer scans of the flat faces indicated that the specimen material had a pronounced texture. For example, the ratio of the intensity of the (0002) peak to that of the (10 $\bar{1}$ 0) peak was 10 times the value expected for completely random orientations. The variation in fracture mode through the thickness of a specimen can be explained if the material has a duplex rolling texture.

The complex shape of the crack front during Stage II crack propagation is illustrated schematically in Figure 28. The crack front consists of the long, narrow cleavage cracks, ("fingers"), which are separated by regions of short cleavage cracks, intergranular cracks, and corrosion pits. This last region of the crack front probably lies behind the long cleavage cracks and offers some resistance to crack extension. It is difficult to comment any more precisely on the propagation of a crack with such a complex geometry. However, these results illustrate two points which are relevant to the interpretation of stress-corrosion experiments.

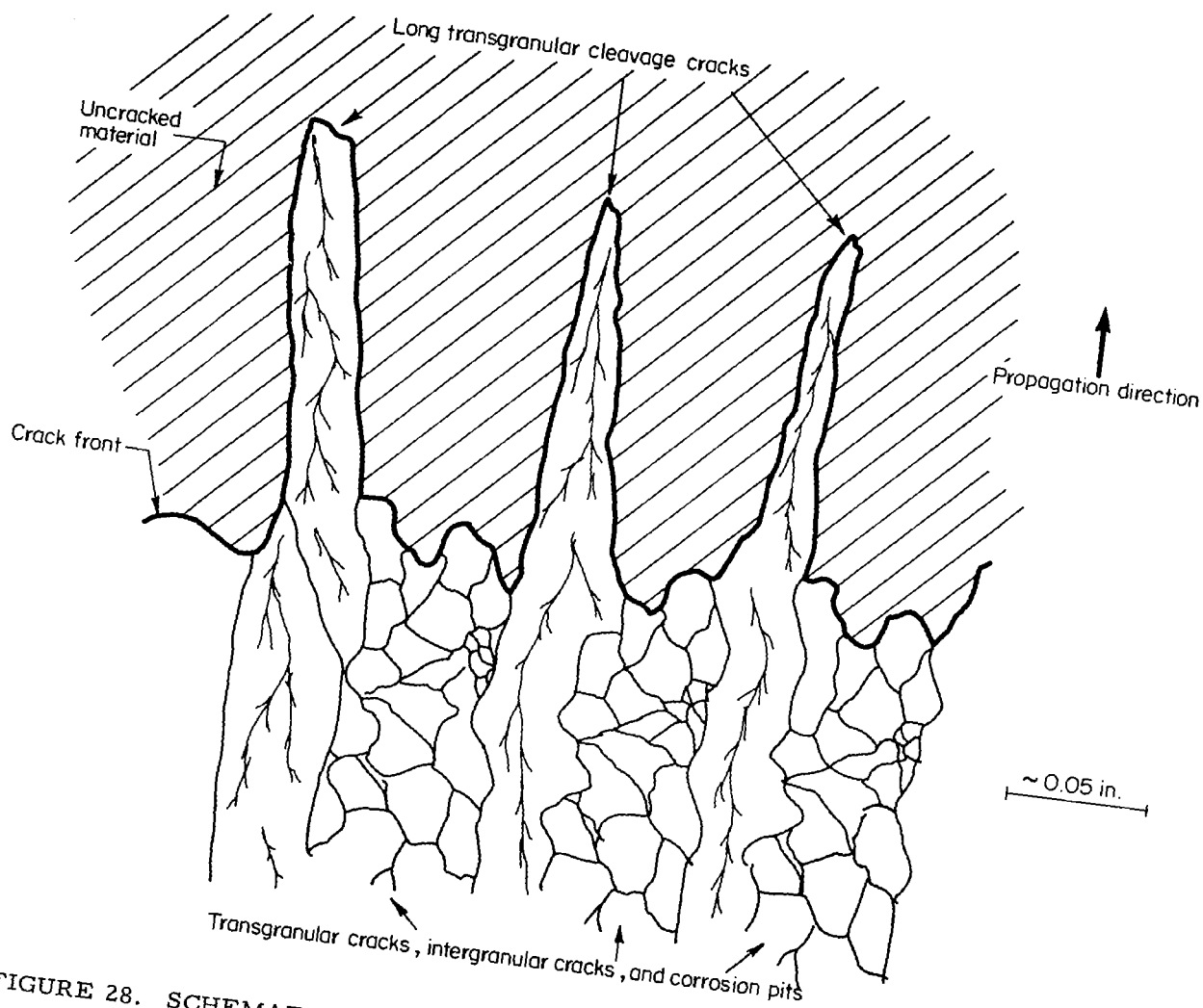


FIGURE 28. SCHEMATIC ILLUSTRATION OF THE FRONT OF A PROPAGATING STRESS CORROSION CRACK DURING STAGE II

- (1) When crack extension involves a combination of electrochemical attack, plastic deformation, and cleavage, fractographic observations can be misleading unless a thorough study over a wide range of magnifications is made. In the present studies, just about every conceivable type of fracture mode could have been reported as "typical" if a sufficiently small area had been examined.
- (2) It is not very meaningful to relate the macroscopic applied stress intensity to the conditions at the tip of a crack with an irregular crack front such as that shown in Figure 28.

Crack-Tip Plastic Zones. The measured size of the plastic zone around the tip of individual crack branches agrees closely with the value calculated from simple elastic-plastic models⁽³⁾. For plane-stress conditions $\rho \approx \pi/8 (K/Y)^2$. For $K = 20 \text{ ksi}\sqrt{\text{in.}}$ and $Y = 150 \text{ ksi}$, calculated value of ρ is 180 microns, which is close to the measured value of 250 microns. However, the size of the plastic zone should increase with increasing stress intensity, but this was not observed. The accuracy of this measurement was such that a change in ρ should have been detected over the range of (K/Y) values investigated. Similarly, the average slip-step height or slip-band spacing also showed no systematic variation with applied stress intensity (Table 9). These observations suggest that either the yield stress of the material ahead of a crack tip is increased during subcritical cracking, or the local stress intensity does not increase continuously with increasing applied stress intensity. The latter explanation is favored in view of the observation of pronounced crack branching at the higher stress intensities. Johnson and Halloway⁽²⁰⁾ have proposed that for supercritical cracking, branching will occur when the strain-energy-release rate is sufficient to create four, rather than two, new surfaces, i. e., $K_{IB} = \sqrt{2} K_{IC}$. Applying this reasoning to subcritical cracking results in the prediction that crack branching should occur when $K_{IB} = \sqrt{2} K_{ISCC}$. Furthermore, the local stress intensity at the tip of an individual crack segment should not exceed K_{IB} ; otherwise, it would branch again into two additional segments. The experimental observations are consistent with this model. At low applied stress intensities, when there is a single crack front, the measured plastic-zone size is close to the expected value. Severe crack branching is observed at higher applied stress intensities, and K_{IB}/K_{ISCC} is estimated to be in the range 1.1 to 2.0. When the propagating crack is branched, the crack velocity, plastic-zone size, and distribution of strain in the plastic zone (as indicated by the measurements of slip offsets and slip-band spacings) are essentially unchanged as the applied stress intensity increases. This illustrates an important distinction between environment-induced subcritical cracking and supercritical cracking. In the case of subcritical cracking, whether or not crack extension occurs is determined by the conditions at the tip of an individual crack segment (or in the small volume of material surrounding it if some embrittling species from the environment can diffuse into the material). On the other hand, the onset of supercritical cracking is determined by the distribution of stress or strain over a much larger volume of material around the whole crack front. Thus, it is possible for subcritical cracking to occur such that the local stress intensity at the tips of individual crack segments remains constant at K_{IB} , which is less than K_{IX} , but when the applied stress intensity (calculated assuming a single crack front) reaches K_{IX} , rapid fracture will occur.

Despite the considerable scatter in the measurements, the slip-band studies provide useful quantitative data about the distribution of slip and the heights of slip offsets in the vicinity of a propagating stress-corrosion crack. These data could be

used as input for the electrochemical models⁽⁵⁾ to evaluate the kinetics of the various reactions that occur in the crack-tip region. However, it must be remembered that the slip-line observations were of necessity made on the surface of the specimen, whereas it is likely that the processes that lead to environment-induced crack extension occur in the plane-strain region in the middle of the specimen. Much of the fracture of the surface layers probably occurs by ductile tearing due to overload. Indeed, many of the fractures seen in the replicas, such as the grain-boundary cracks in Figure 18, are similar to what is observed to accompany ductile rupture of smooth tensile specimens in air⁽²³⁾.

N₂O₄ Environments

Chemical Studies

A number of experimental alloys of between 5 to 7 weight percent aluminum (Table 12) and containing varying additions of molybdenum, vanadium, and oxygen, were exposed to oxygenated (red) N₂O₄. The 6.5 to 7 Al-base alloys (designated as second-year-study alloys) were exposed in the form of 60-mil-thick machined sheet specimens stressed at 90 percent of their 0.2 percent offset yield stress by constant deflection in stainless steel three-point-loading fixtures and in the form of U-bends. Both types of specimens were placed in 1-liter glass-lined autoclaves containing 500 ml green N₂O₄ and pressurized to 250 psig with O₂. The specimens were exposed for a period of 7 days at a temperature of 106 F. It was found that all of the three-point-loaded and U-bend specimens failed by cracking in the region of maximum stress.

TABLE 12. COMPOSITION, WEIGHT PERCENT,
OF EXPERIMENTAL ALLOYS
EXPOSED TO N₂O₄

Ti-7Al-1.5Mo-0.5V-0.05 O
Ti-7Al-1.5Mo-0.5V-0.1 O
Ti-7Al-1.5Mo-0.5V-0.23 O
Ti-7Al-1.5Mo-0.5V-0.10-0.2Pd
Ti-7Al-2Mo-0.1 O
Ti-7Al-3Mo-1V-0.1 O
Ti-7Al-2V-0.1 O
Ti-7Al-0.1 O
Ti-7Al-2Mn-0.1 O
Ti-6.5Al-1.5Mo-0.5V-0.05 O
Ti-6.5Al-1.5Mo-0.5V-0.1 O
Ti-6.5Al-1.5Mo-0.5V-0.22 O
Ti-6Al-1.5Mo-0.5V-0.05 O
Ti-6Al-1.5Mo-0.5V-0.1 O
Ti-6Al-1.5Mo-0.5V-0.18 O
Ti-6Al-0.1 O
Ti-6Al-2Mo-0.1 O
Ti-6Al-2V-0.1 O
Ti-6Al-4V-0.1 O
Ti-5.5Al-1.5Mo-0.5V-0.1 O
Ti-5Al-1.5Mo-0.5V-0.1 O

As observed in previous work, all alloys with the exception of the Ti-7Al-1.5Mo-0.5V-0.23 O and Ti-7Al-2Mn-0.1 O showed the presence of purple and/or golden colored films on the fracture faces. Specimens from this study were used for metallography and also for SEM fractographic studies described later.

The 5 to 6Al-base alloys (designated as alloys of the third-year study) were also exposed to oxygenated (red) N_2O_4 . The alloys, in the form of 60-mil-thick sheet specimens, were exposed as bend specimens in 500 ml green N_2O_4 pressurized to 250 psig with O_2 at 104 F for a period of 6 days. Upon removal, all specimens were found to have failed because of cracks at the apex of the U-bends. In the majority of specimens, there was a large number of cracks. Some slight staining was noticed around the edges of the cracks.

In addition to exposure of stressed specimens of the experimental alloys, the same alloys have been exposed in the unstressed condition to oxygenated (red) N_2O_4 . The unstressed specimens were exposed in the as-machined condition. The weight-loss data for these alloys are summarized in Table 13. Examination of the alloys after exposure revealed the presence of transverse cracks in all of the specimens. These cracks appeared to be transgranular and penetrated to a depth between 2 and 3 mils. Similar cracks were not observed, however, on some machined specimens which had been given a '600' metallographic polish. This suggests that such surface cracks had probably occurred as the result of a cold-worked layer from machining. The presence of such microcracks could have influenced the general weight-loss data slightly but, as seen from the data in Table 13, some trends are evident. The results show that (1) the α/β alloy Ti-7Al-2Mn-0.1 O was the most corrosion resistant of the alloys studied and was followed in decreasing order of corrosion resistance by the α alloys Ti-7Al-0.1 O and Ti-6Al-0.1 O and the α/β alloys Ti-7Al-2V-0.1 O and Ti-6Al-2V-0.1 O; (2) in the 6 and 7Al-base alloys the poorest corrosion resistance was observed for those with the highest molybdenum content, i. e., Ti-7Al-3Mo-1V-0.1 O, Ti-7Al-2Mo-0.1 O, and Ti-6Al-2Mo-0.1 O; (3) in a series of alloys of otherwise similar composition, the corrosion resistance decreased with an increase in oxygen content and also with an increase in vanadium content.

The effect of manganese and oxygen on corrosion resistance is not fully understood. However, the decrease in corrosion resistance with increasing molybdenum or vanadium additions is not unexpected since these elements reduce the resistance of other alloy systems in highly oxidizing environments. It should be noted that variations in the aluminum content between 5 and 7 percent did not significantly affect the corrosion behavior of the experimental alloys.

Electron-probe microanalyses were attempted on commercial-type Ti-6Al-4V alloy in the annealed condition to determine the composition of the α and β grains. The study was conducted since it was believed that these compositional data and the analysis of the postfailure N_2O_4 solution in which Ti-6Al-4V specimens cracked could indicate which metallic phase is most susceptible to dissolution during cracking. An analysis of an N_2O_4 solution in which Ti-6Al-4V alloy specimens had cracked revealed 30 parts V:7 parts Al which is greater than the mean composition of 4 parts V:6 parts Al. The analysis, therefore, suggests that the β phase of this alloy may be most susceptible to dissolution. The electron-probe microanalyses were inconclusive, however, because of the small grain size of the alloy, which resulted in a mean analysis of α and β grains. The sensitivity of the analysis was not improved by annealing the alloys at 1400 F for a period of 30 hours to increase the grain size slightly.

TABLE 13. WEIGHT LOSS OF TITANIUM ALLOYS EXPOSED TO
OXYGENATED N_2O_4 AT 250 PSIG O_2 AND 106 F

Alloy Composition, weight percent					Weight Loss, mg/dm ² /day
Al	Mo	V	O	Other	
7	1.5	0.5	0.05		2.1
7	1.5	0.5	0.1		3.8
7	1.5	0.5	0.23		4.1
7	1.5	0.5	0.1	0.2Pd	3.0
7	2	--	0.1		5.9
7	3	1	0.1		6.5
7	--	2	0.1		0.5
7	--	--	0.1		0.3
7	--	--	0.1	2Mn	<0.1
6.5	1.5	0.5	0.05		4.5
6.5	1.5	0.5	0.1		3.3
6.5	1.5	0.5	0.22		3.8
6	1.5	0.5	0.05		3.3
6	1.5	0.5	0.1		2.9
6	1.5	0.5	0.18		5.5
6	2	--	0.1		5.9
6	--	2	0.1		1.9
6	--	4	0.1		3.4
6	--	--	0.1		0.6
5.5	1.5	0.5	0.1		3.2
5	1.5	0.5	0.1		1.7

Electrochemical Studies

Previous work with the type Ti-6Al-4V alloy had led to a proposed mechanism⁽²²⁾ for the stress-corrosion cracking of this alloy in oxygenated (red) N_2O_4 . This mechanism was based in part upon the highly positive (noble) potential value of 1.0 to 1.3 volts versus SHE of the material during cracking and the strong influence of oxygen on the cracking behavior. It was believed that the influence of anodic and cathodic polarization on the cracking behavior of this alloy might provide valuable mechanistic data.

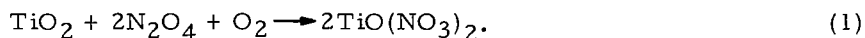
A series of experiments were conducted in which U-bend specimens of the type Ti-6Al-4V alloy in the STA condition were made anodic and cathodic in oxygenated (red) N_2O_4 . Electrical leads were made available to the specimens inside the autoclave through the use of Conax fittings in the autoclave head. Dry batteries were used as a d-c source for supplying polarization current. All experiments were conducted in a 1-liter autoclave containing 250 ml green N_2O_4 such that the U-bend specimens were just covered. The autoclaves were pressurized to 250 psig with O_2 and the experiments conducted at 106 F.

In the first experiment, two U-bend specimens were supported adjacent in upright positions with the planes of the specimens parallel and 0.85 inch apart. One specimen was made anodic and the other was made cathodic. It was found that 450 volts dc was necessary to produce a current density of 2.0×10^{-8} amp/in.². After 3 days the current had decreased to 1.3×10^{-8} amp/in.² and the experiment was stopped. Examination of the specimens indicated that both had failed because of large cracks and many secondary cracks at the apex of the U-bends. It appeared that the cathodically polarized specimen had slightly more secondary cracks than did the anodically polarized specimen. However, neither the cathodic nor anodic polarization appeared to significantly influence the cracking behavior in this experiment. It is possible that currents were too small to influence the cracking behavior and/or the current distribution to the apex of the U-bends was poor.

In the second experiment, two U-bend specimens were placed in the horizontal position with the apex of the specimens adjacent and 0.25 inch apart. On application of 450 volts dc, a current density of 9.0×10^{-7} amp/in.² was attained, but this decreased to 1.5×10^{-7} amp/in.² in 3 days. Upon removal after 3 days, it was found that both specimens had microcracks at the apex of the U-bends. The anode specimen was found to be dull and covered with a gray film. The cathode, on the other hand, was still bright and again appeared to contain the greater number of cracks. The decrease in current with exposure time was probably related to the thickening of a poorly conducting oxide film of TiO₂ on the anode. The formation of this anodic film and consequent decrease in current was reproduced in a further experiment of shorter duration.

The experiments indicated that anodic polarization slightly reduced the number of secondary cracks associated with the stress-corrosion cracking. At the values of anodic polarization employed, however, the stress-corrosion cracking process could not be totally arrested. Larger anodic polarization rates could not be readily carried out since anodic film formation decreased the polarization current. By employing a platinum anode, it was possible to conduct an experiment in which a type Ti-6Al-4V U-bend was polarized at an initial cathodic rate of 5.2×10^{-5} amp/in.², but this rate decreased to 6.4×10^{-7} amp/in.² in less than 16 hours as a result of the filming of the platinum anode. After 4-1/2 days' exposure, the U-bend specimen was completely cracked and contained numerous secondary cracks. Large amounts of cathodic polarization, therefore, did not appear to be beneficial in arresting stress-corrosion cracking.

The large amount of voltage required to impress even small polarization currents in this environment and the ineffectiveness of the polarization to arrest stress-corrosion cracking indicated that typical electrochemical processes are probably not of major importance in the stress-corrosion cracking mechanism of titanium in N₂O₄. The film formation of, probably, TiO₂ during anodic polarization was successful in decreasing the number of secondary cracks. This result implies that film breakdown and/or formation of a nonprotective film by chemical means is probably the important process in the stress-corrosion cracking mechanism. The result is thus in accord with the proposed mechanism⁽²²⁾ in which an unprotective TiO(NO₃)₂ film is postulated to occur by means of the reaction



Fractographic Studies

A major part of the year's work has been concerned with fractographic studies to identify the relationship between composition of the alloys and their stress-corrosion-cracking behavior in oxygenated (red) N_2O_4 . On the whole, these studies have been conducted using scanning electron microscopy (SEM). All of the alloys have been investigated with regard to mode of fracture in the main fracture plane. The 6.5 to 7Al-base second-year alloys, however, have also been investigated with regard to fractographic features on the outer surface of the alloys, i.e., the initiating surface, and also with regard to cross-sectional metallography.

Surface fractographic studies of cracked specimens were conducted to determine features and phases most susceptible to stress-corrosion cracking. These studies were conducted with the 6.5 to 7Al-base second-year alloys, Ti-6Al-4V alloy in the STA condition and unalloyed Ti-75A. In order to allow the surface features of cracked specimens to be studied by microscopy, it was necessary to etch polish the specimens prior to exposure. Machined sheet specimens (4.5 x 0.5 x 0.060 inch) normally used for three-point loading and U-bend specimens were given an electrolytic, anodic etch-polish treatment. An unmasked area of 1 cm² in the middle of the specimen was etch polished at 2 amp/cm² and 30 volts in a solution⁽²³⁾ containing 295 cc CH₃OH, 175 cc n-C₄H₉OH, and 30 cc HClO₄, and cooled in a carbon dioxide-acetone bath. After etch polishing, the specimens were made into U-bends and exposed to oxygenated (red) N_2O_4 at 250 psig O₂ and 106 F for 5 days. Upon removal, all specimens had failed because of cracking. However, Ti-6.5Al-1.5Mo-0.5V-0.22 O, Ti-7Al-1.5Mo-0.5V-0.23 O, and Ti-3Mo-1V-0.1 O had failed because of cracks on the outside of the etch-polished area near the apex of the U-bends and, therefore, these alloys were not used in the surface, fractographic studies.

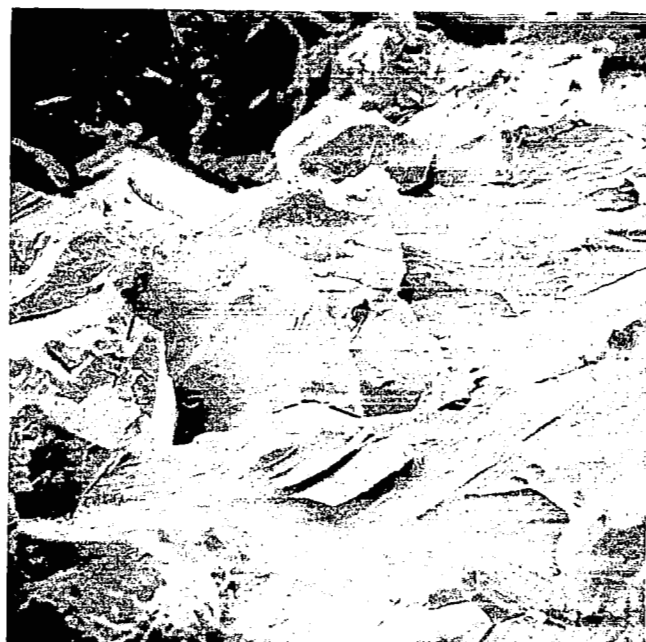
6.5 to 7 Al-Base Alloys. The fracture faces of two α alloys Ti-7Al-0.1 O and unalloyed Ti-75A were quite different. As shown in Figure 29, the Ti-7Al-0.1 O alloy had a predominantly intergranular fracture mode, whereas the Ti-75A, as shown in Figure 30, evidenced both intergranular and transgranular, i.e., mixed mode of cracking. These same modes of cracking were reflected in the metallographic study (Figure 31) of the Ti-7Al-0.1 O alloy and surface fractography study (Figure 32) of the Ti-75A alloy. It is interesting to note that the small amount of approximately 0.35 weight percent oxygen present in Ti-75A is sufficient to bring about a marked amount of brittle cleavage fracture in this α alloy. Examination of the intergranular cracks of the Ti-7Al-0.1 O alloy indicated that localized attack in the form of pitting (Figure 33) probably occurred prior to complete dissolution of the grain-boundary area. The localized attack at the grain boundary area may be due to inhomogeneity within the alloy at the pitted sites. The sites of inhomogeneity are preferentially dissolved in the N_2O_4 environment.

Examination of the fracture faces of the Ti-6.5Al-1.5Mo-0.5V and Ti-7Al-1.5Mo-0.5V α/β alloys clearly indicated that increasing the amount of oxygen addition to these alloys produced an increase in the proportion of transgranular fracture mode in the alloys. This behavior is illustrated in Figures 34 and 35 for the Ti-6.5Al-base alloys. As shown in Figure 36, a typical alloy in this series showed that on the surface, transgranular cracking appeared to be preferred to dissolution of the α or β phase. Photomicrography, however, identified both transgranular cracking and cracks at the α/β grain boundaries below the surface for this series of alloys, as shown by Figure 9 for the Ti-7Al-1.5Mo-0.5V-0.23 O material. The addition of 0.2Pd in this same series of alloys produced a marked transgranular fracture mode (Figure 38) similar



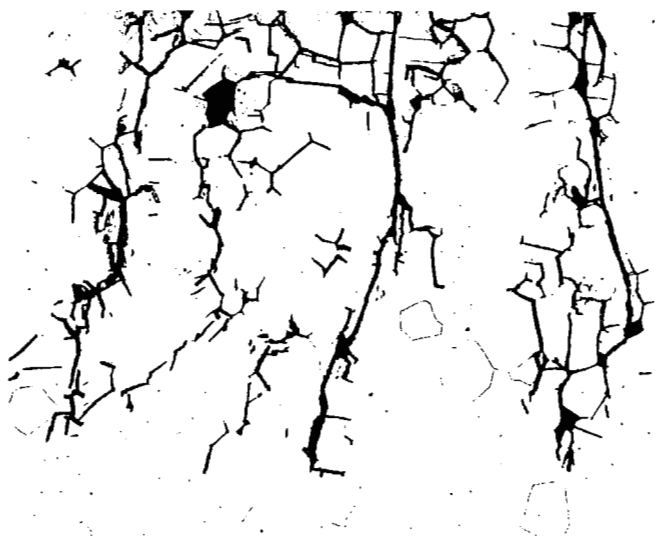
500X

FIGURE 29. SEM FRACTOGRAPH OF
Ti-7Al-0.1 O ALLOY



500X

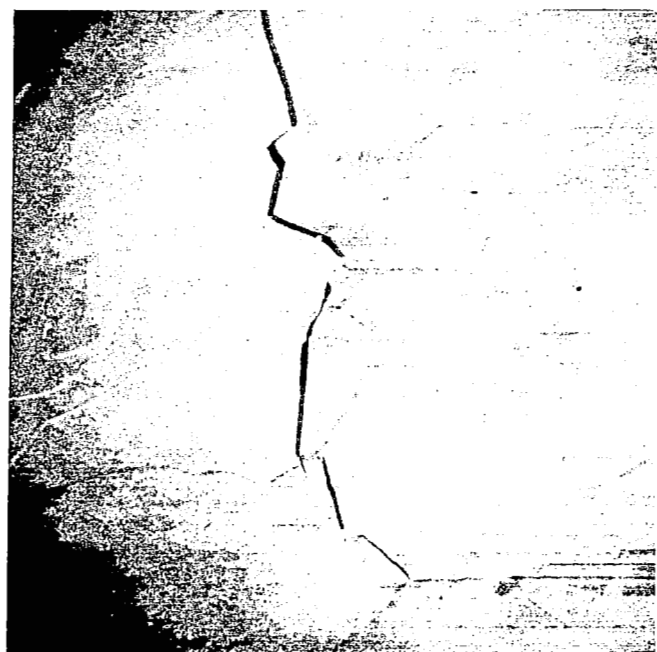
FIGURE 30. SEM FRACTOGRAPH OF
Ti-75A ALLOY



100X

Etched

FIGURE 31. PHOTOMICROGRAPH OF
Ti-7Al-0.1 O ALLOY



500X

FIGURE 32. SURFACE FRACTOGRAPH
OF Ti-75A ALLOY



10,000X

FIGURE 33. SEM SURFACE PHOTOMICROGRAPH OF
Ti-7Al-0.1 O ALLOY



2000X

FIGURE 34. SEM FRACTOGRAPH OF
Ti-6.5Al-1.5Mo-0.5V-
0.1 O ALLOY



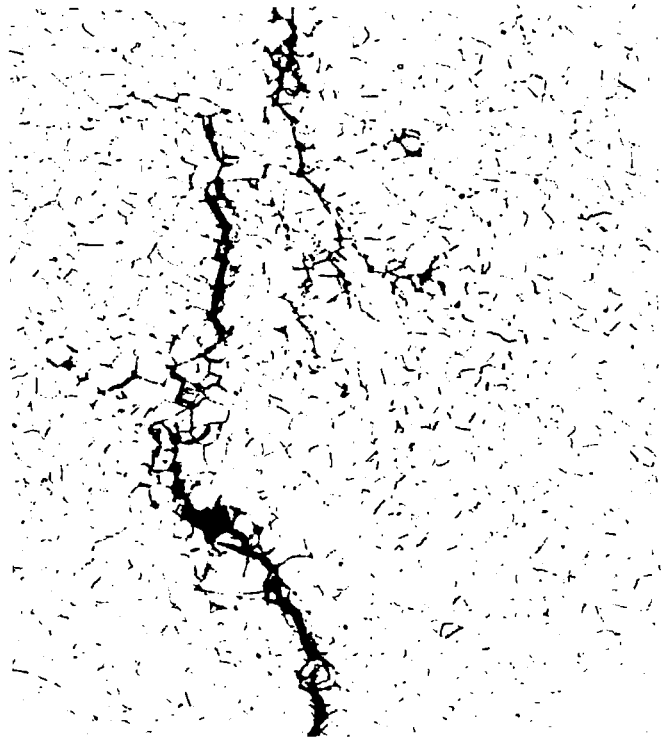
2000X

FIGURE 35. SEM FRACTOGRAPH OF
Ti-6.5Al-1.5Mo-0.5V-
0.22 O ALLOY



5000X

FIGURE 36. SEM SURFACE FRACTOGRAPH OF Ti-7Al-1.5Mo-0.5V-0.1 O ALLOY



500X

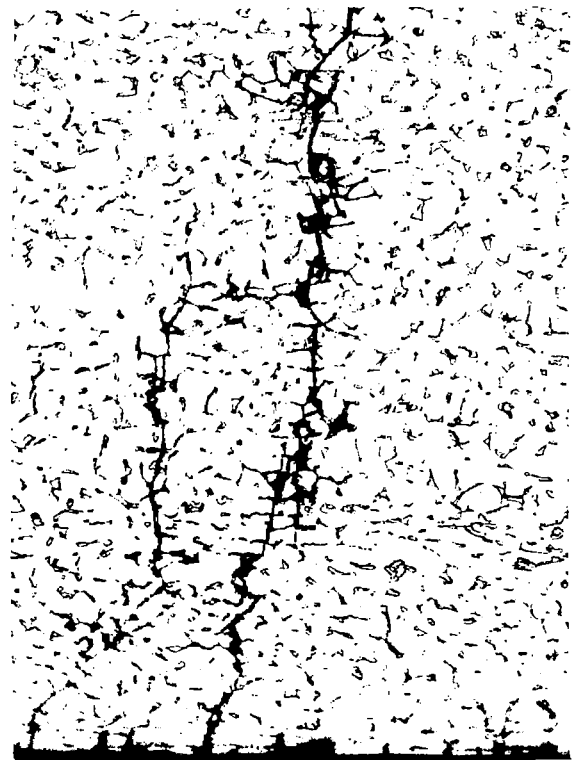
Etched

FIGURE 37. PHOTOMICROGRAPH OF Ti-7Al-1.5Mo-0.5V-0.23 O ALLOY



2000X

FIGURE 38. SEM FRACTOGRAPH OF Ti-7Al-1.5Mo-0.5V-0.2Pd ALLOY



500X

FIGURE 39. PHOTOMICROGRAPH OF Ti-7Al-1.5Mo-0.5V-0.2Pd ALLOY

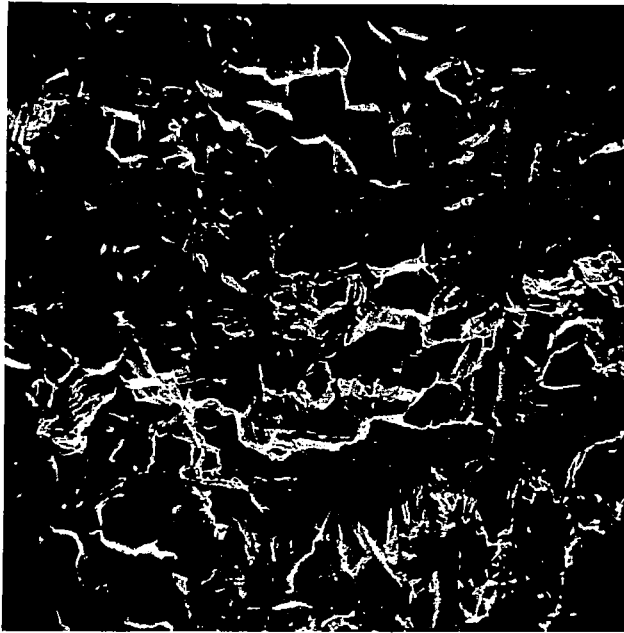
to that obtained by oxygen additions. This fracture mode was further evidenced in metallographic studies from which it was also noted that cracking was apparently associated with pits at the surface (Figure 39). The fractures of the Ti-7Al-3Mo-1V-0.1 O and Ti-7Al-2Mo-0.1 O alloys were very similar in appearance and were predominantly transgranular and similar to the fracture shown in Figure 35 for the Ti-6.5Al-1.5Mo-0.5V-0.22 O alloy. The Ti-7Al-2V-0.1 O alloy, which has a relatively small β content, revealed a fracture face with very discrete areas of both intergranular and transgranular cleavage fracture mode as shown in Figure 40. On the other hand, the Ti-7Al-2Mn-0.1 O alloys which also have a relatively small β content, gave a fracture with some evidence of ductility, as shown in Figure 41. Although all the alloys exhibited some ductile fracture mode near the area of final separation, the Ti-7Al-2Mn-0.1 O alloy was the only material to show this behavior at early stages of fracture. This behavior suggests a slow-moving cracking such that some plastic deformation has time to occur around the moving crack tip. The slow cracking behavior of this alloy, together with its corrosion resistance, indicates an alloy composition that is probably the most resistant to stress-corrosion cracking in oxygenated (red) N_2O_4 .

The Ti-6Al-4V alloy in the STA condition appeared to show predominant transgranular fracture mode, but this was not easily recognized because of corrosion product on the surface (Figure 42). Metallographic examination of the alloy also indicated a transgranular fracture mode, but in addition, appeared to indicate attack of the β phase adjacent to the crack (Figure 43). This attack of the β phase was not noted from surface studies, although it did appear that the α/β grain boundaries were attacked (Figure 44). The fracture mode at the surface was also predominantly transgranular.

5 to 6 Al-Base Alloys. The same compositional effects noted for the 6.5 and 7 Al-base alloys were continued in the 5 and 6 Al-base alloys of the third-year study as illustrated below.

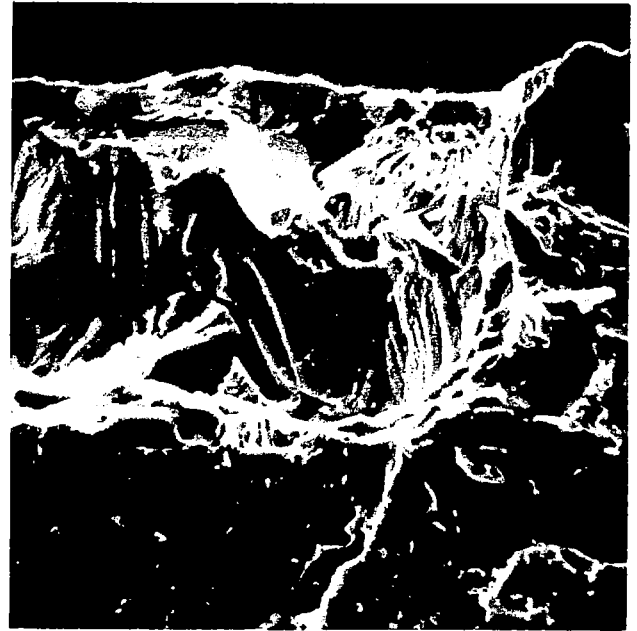
The α alloy Ti-6Al-0.1 O exhibited a predominantly intergranular fracture mode (Figure 45) similar to Ti-7Al-0.1 O. Pits on the surface of this material were associated with some of the transgranular fracture behavior in this alloy and thus may represent crack initiation sites.

As observed for the 6.5 and 7 Al-base alloys, an increase in oxygen content from 0.05 to 0.18 weight percent in the Ti-6Al-1.5Mo-0.5V and Ti-6.5Al-1.5Mo-0.5V series of alloys produced an increasing proportion of transgranular-cleavage fracture mode. At a concentration of 0.05 oxygen in this series of alloys, there were subtle, although not very significant, differences to suggest that the proportion of transgranular fracture mode increased with increasing aluminum content from 5 to 7 weight percent. The effect was more marked at the 0.18 to 0.23 oxygen concentration, but could be accounted for by the changes in oxygen concentration rather than the aluminum content. Such effects of aluminum on fracture mode would be difficult to understand. At the concentration of 0.1 oxygen in this series of alloys, it was observed that the proportion of transgranular fracture mode decreased with increase in aluminum content from 5 to 6.5 weight percent. This behavior is illustrated by comparison of Figures 34, 46, and 47. The same effect has been noted for the Ti-6Al-2V-0.1 O alloy which had a more predominant transgranular fracture mode than did its 7Al-base counterpart (compare Figure 48 with Figure 40). The effect was not so pronounced for the Ti-6Al-2Mo-0.1 O and Ti-7Al-2Mo-0.1 O alloys. The reason for the intermediate level of oxygen at 0.1 weight percent altering the influence that aluminum has on fracture mode at other levels is not fully understood. The results imply a change in the role of oxygen at this intermediate level.



500X

FIGURE 40. SEM FRACTOGRAPH OF
Ti-7Al-2V-0.1 O ALLOY



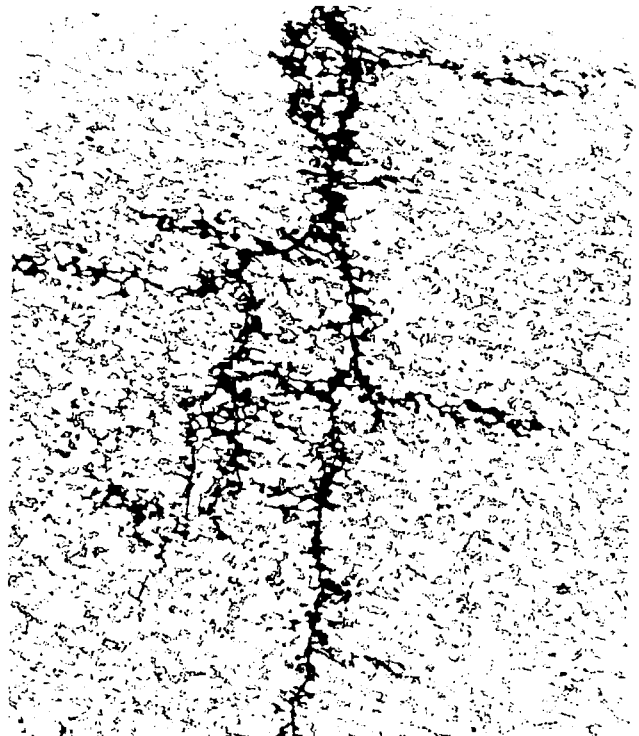
2000X

FIGURE 41. SEM FRACTOGRAPH OF
Ti-7Al-2Mn-0.1 O ALLOY



2000X

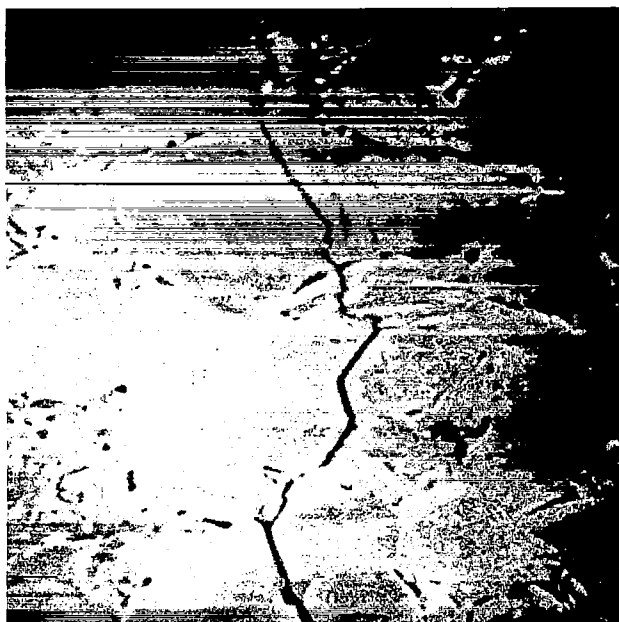
FIGURE 42. SEM FRACTOGRAPH OF Ti-6Al-4V ALLOY
IN THE STA CONDITION



500X

Etched

FIGURE 43. PHOTOMICROGRAPH OF Ti-6Al-4V ALLOY
IN THE STA CONDITION



5000X

FIGURE 44. SEM SURFACE FRACTOGRAPH OF Ti-6Al-4V ALLOY
IN STA CONDITION



5000X

FIGURE 45. SEM FRACTOGRAPH OF
Ti-6Al-0.1 O ALLOY



2000X

FIGURE 46. SEM FRACTOGRAPH OF
Ti-6Al-1.5Mo-0.5V-0.1 O
ALLOY



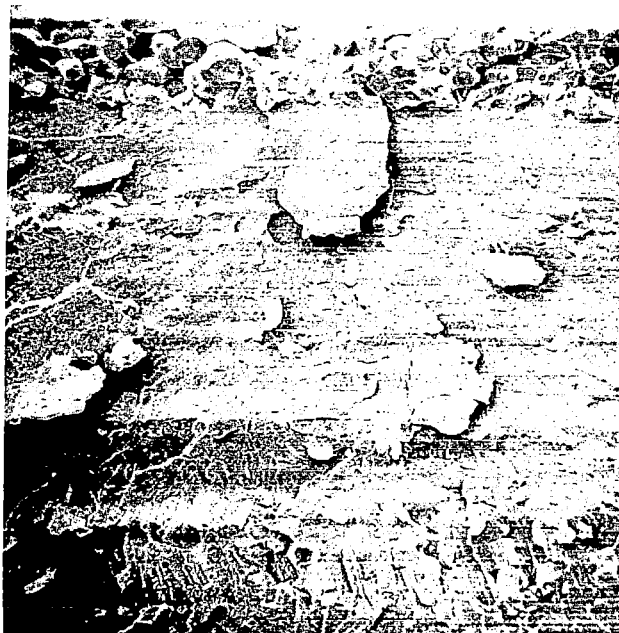
2000X

FIGURE 47. SEM FRACTOGRAPH OF
Ti-5Al-1.5Mo-0.5V-
0.1 O ALLOY



500X

FIGURE 48. SEM FRACTOGRAPH OF
Ti-6Al-2V-0.1 O ALLOY



500X

FIGURE 49. SEM FRACTOGRAPH OF Ti-6Al-1.5Mo-0.5V-
0.18 O ALLOY

No major differences were found in the fracture behavior of laboratory Ti-6Al-4V alloy and commercial Ti-6Al-4V alloy in the STA condition. Figure 45 shows an interesting fracture feature of the Ti-6Al-1.5Mo-0.5V-0.18 O alloy. The initial and very predominant intergranular fracture mode changes to a transgranular cleavage fracture mode as the stress intensity at the root of the crack increases beyond a value necessary to initiate a cleavage fracture. The absence of any ductile characteristics in the fracture indicates a very fast brittle cleavage fracture.

Summary

Fractographic, chemical, and electrochemical studies have been employed to study the effects of composition of the 5 to 7Al-base experimental alloys (Table 12) on their stress-corrosion cracking behavior in oxygenated (red) N_2O_4 .

All of the experimental alloys exhibited stress-corrosion cracking in oxygenated (red) N_2O_4 at 250 psig O_2 and 106 F. Alloy composition was found to markedly influence the corrosion resistance and stress-corrosion-cracking fracture mode of the alloys in oxygenated (red) N_2O_4 .

Corrosion resistance was found to decrease with increasing additions of molybdenum, vanadium, and oxygen. The effect of molybdenum and vanadium, thus, typified the general corrosion behavior of these alloying elements in oxidizing environments. Aluminum content had no significant effect on the corrosion resistance of the alloys, but the α alloys Ti-6Al-0.1 O and Ti-7Al-0.1 O did show good corrosion resistance. The most corrosion-resistant alloy was Ti-7Al-2Mn-0.1 O. This alloy, which also indicated an initial slow crack growth, represented the most resistant alloy to stress-corrosion cracking in the oxygenated (red) N_2O_4 .

With the exception of the α alloys Ti-6Al-0.1 O and Ti-7Al-0.1 O, which evidenced a marked intergranular fracture mode, the α/β alloys generally exhibited mixed intergranular/transgranular fracture modes. It is apparent that increasing the amount of the additions of oxygen and vanadium in the Ti-Al-Mo-V-O alloys increased the proportion of transgranular cleavage fracture mode. Oxygen additions were most marked in producing this behavior. A palladium addition was also found to increase the proportion of transgranular cleavage fracture mode. The Ti-7Al-2Mn-0.1 O alloy was the only alloy in which some ductile character in the early fracture stages was observed. This is indicative of slow crack growth.

The decrease in corrosion resistance paralleled the increasing proportion of transgranular cleavage fracture mode in the stress-corrosion cracking of the alloys. It appears, therefore, that the above alloy additions which promote transgranular cleavage fracture may do so by aiding production of a brittle phase within the grains which is also chemically active. Such an embrittling phase might be Ti_3Al since it is believed that increased additions of aluminum and oxygen to Ti-Al alloys favor its formation⁽²⁴⁾. However, the β stabilizers vanadium and molybdenum are believed to decrease the amount of Ti_3Al formed, which does not support the hypothesis. This suggests that chemical activity may arise through dissolution of the β phase as well as the embrittling Ti_3Al phase. Such reactivity of the β phase has been observed in the Ti-6Al-4V alloy, which has a relatively high β content.

Polarization studies on Ti-6Al-4V alloy have indicated that the electrochemical reactions are probably not the most important processes in this poorly conducting environment. Results indicated that anodization which probably gives rise to a thickening of the TiO_2 film can slow down the stress-corrosion-cracking process. The localized breakdown of the oxide film and its inability to repair as postulated in the proposed mechanism⁽²⁴⁾ is probably the most important factor.

REFERENCES

- (1) Boyd, J. D., Moreland, P. J., Boyd, W. K., Wood, R. A., Williams, D. N., and Jaffee, R. I., "The Effect of Composition on the Mechanism of Stress-Corrosion Cracking of Titanium Alloys in N_2O_4 and Aqueous and Hot-Salt Environments", National Aeronautics and Space Administration, Contractor Report No. CR-1525, February, 1970.
- (2) Brown, B. F., "A New Stress-Corrosion-Cracking Test Procedure for High-Strength Alloys", *Mat. Res. Std.*, 6, 129 (1966).
- (3) Hahn, G. T., and Rosenfield, A. R., "Sources of Fracture Toughness: The Relation Between K_{Ic} and the Ordinary Tensile Properties of Metals", ASTM STP432, p 5 (1968).
- (4) Blackburn, M. J., et al., "State of the Art of Stress-Corrosion Cracking of Titanium Alloys", Boeing Company Report, June, 1970.
- (5) Beck, T. R., "Electrochemical Aspects of Titanium Stress Corrosion Cracking", in Fundamental Aspects of Stress Corrosion Cracking, R. W. Staehle et al. (Eds.), NACE, Houston (1969), p 605.
- (6) Latanision, R. M., and Staehle, R. W., "Stress Corrosion Cracking of Iron-Nickel-Chromium Alloys", *ibid*, p 214.
- (7) Pugh, E. N., et al., "The Stress-Corrosion Cracking of Copper, Silver, and Gold Alloys", *ibid*, p 118.
- (8) Blackburn, M. J., and Williams, J. C., "Metallurgical Aspects of the Stress-Corrosion Cracking of Titanium Alloys", *ibid*, p 620.
- (9) Piper, D. E., and Feeney, J. A., ARPA Coupling Program on Stress-Corrosion Cracking, Eleventh Quarterly Report, July, 1969, p 6.
- (10) Rostoker, W., et al., Embrittlement by Liquid Metals, Reinhold, New York (1960).
- (11) Brown, B. F., Fujii, C. T., and Dahlbery, E. P., *J. Electrochem. Soc.*, 116, 218 (1969).
- (12) Hahn, G. T., and Rosenfield, A. R., "Experimental Determination of Plastic Constraint Ahead of a Sharp Crack Under Plane-Strain Conditions", *Trans. ASM*, 59, 909 (1966).
- (13) Katz, Y., and Gerberich, W. W., *Int. J. Fracture Mech.*, 6, 219 (1970).
- (14) Wiederhorn, S. M., "Moisture-Assisted Crack Growth in Ceramics", *Int. J. Fracture Mech.*, 4, 171 (1968).

- (15) Carter, C. S., "Stress-Corrosion Crack Branching in High-Strength Steels", Boeing publication D6-23871, March, 1969.
- (16) Speidel, M. O., "Effect of Stress and Environment on Velocity and Branching of Subcritical Cracks", paper presented at AIME Spring Meeting, Las Vegas, Nevada, May, 1970.
- (17) Kies, J. A., et al., "Fracture Testing of Weldments", ASTM STP381, p 328 (1965).
- (18) Meyn, D. A., and Sandoz, G., "Fractography and Crystallography of Subcritical Crack Propagation in High-Strength Titanium Alloys", Trans. AIME, 245, 1253, (1969).
- (19) Mauney, D. A., and Starke, E. A., "Explanation of the Cleavage Plane in Stress-Corrosion Cracking of Alpha Phase Titanium-Aluminum Alloys", Corrosion, 25, 179 (1969).
- (20) Johnson, J. W., and Holloway, D. G., "On the Shape and Size of Fracture Zones on Glass Fracture Surfaces", Phil. Mag., 14, 731 (1966).
- (21) Boyd, J. D., and Hoagland, R. G., "The Relation Between Surface Slip Topography and Stress-Corrosion Cracking in Ti-8 wt % Al", presented at the International Symposium on Stress-Corrosion Mechanisms in Titanium Alloys", to be published by N. A. C. E.
- (22) Moreland, P. J., and Boyd, W. K., Corrosion, 26, 153 (1970).
- (23) Sanderson, G., and Scully, J. C., Corrosion, 24, 75 (1968).
- (24) Lane, I. R., and Cavallero, J. L., "Metallurgical and Mechanical Aspects of the Sea-Water Stress Corrosion of Titanium", ASTM STP432, p 147 (1968).